

Autonomous Horizon-based Asteroid Navigation With Observability-constrained Maneuvers

Aditya A. Anibha^{1*} and Kenshiro Oguri²

¹School of Aeronautics and Astronautics, Purdue University, West Lafayette, Indiana, 47906, USA.

²School of Aeronautics and Astronautics, Purdue University, West Lafayette, Indiana, 47906, USA.

*Corresponding author(s). E-mail(s): aanibha@purdue.edu;
Contributing authors: koguri@purdue.edu;

Abstract

Asteroid exploration is a pertinent challenge due to the varying complexity of their dynamical environments, shape, and communication delays due to distance. Thus, autonomous navigation methods are continually being developed and improved in current research to enable their safe exploration. These methods often involve using Optical Navigation (OpNav) to determine the spacecraft's location, which relies on the horizon's visibility. It is critical to ensure the reliability of this measurement so that the spacecraft may maintain an accurate state estimate throughout its mission. This paper presents an observability-constrained algorithm that generates orbital maneuvers for spacecraft to follow trajectories that allow continuously usable optical measurements to maintain system observability for safe navigation. This algorithm improves upon existing asteroid navigation capabilities by allowing the safe and robust autonomous targeting of various trajectories. The algorithm is adaptable to different asteroid scenarios, and allows a spacecraft to orbit at a wide range of distances within the optical measurement range. The paper presents a comprehensive framework that simulates asteroid dynamics, synthetic image generation, edge detection, horizon-based OpNav, filtering, and observability-constrained control.*

Keywords: Asteroid Navigation, Horizon-based Optical Navigation, Extended Kalman Filtering, Lyapunov control, Spacecraft Autonomy, Observability-constrained control

*A preliminary version of this work was previously presented during the 4th Space Imaging Workshop at Georgia Institute of Technology, Atlanta, GA.

1 Introduction

Asteroid exploration has recently gained significant interest, driven by scientific research, resource utilization, and planetary defense purposes. Successful missions, such as *Hayabusa2* to 162173 Ryugu and *OSIRIS-REx* to 101955 Bennu, have provided valuable insights into the composition and structure of these small bodies [1, 2]. However, both missions required extensive observation periods to safely navigate their respective targets' uncertain and weak gravitational environments. For example, *OSIRIS-REx* spent nearly a year mapping Bennu before attempting proximity operations [3], while *Hayabusa2* similarly mapped Ryugu for months [4]. In addition to these missions, the *DART* and *Lucy* missions also emphasize the need for detailed pre-mission observations to ensure safe proximity operations [5, 6]. These missions highlight the need for improvements in autonomous Optical Navigation (OpNav) to reduce the reliance on long observation periods or human-in-the-loop processes to improve mission efficiency and reliability.

OpNav has become a preferred method for space missions due to its reliability, accuracy, and accessibility, particularly when navigating larger spherical bodies like the Moon or Mars [7]. OpNav relies on visual images of celestial bodies, allowing spacecraft to determine their position by analyzing surface features or horizons. Some types of OpNav include surface feature tracking, Line Of Sight (LOS)[8], Central and Apparent Diameter (CAD)[9], Lidar-based[10, 11], Limb-based [12] and Pole-from-Silhouette, Shape-from-Silhouette or Localization-from-Silhouette [13] methods.

In the case of *Hayabusa2*, both human-in-the-loop and autonomous OpNav are used extensively throughout the mission, from approach to landing and sample collection phases at asteroid 162173 Ryugu. The spacecraft employed a series of optical images captured by its onboard OpNav Camera (ONC) to estimate its position and velocity relative to the asteroid's surface. This information is crucial for accurately guiding the spacecraft during its low-altitude descents and surface interactions. In addition, OpNav is used during the mission's descent to provide detailed images of Ryugu's surface, enabling the mission team to select safe landing sites. The mission relied heavily on OpNav for proximity operations, including final descent and collection maneuvers, illustrating its importance in achieving mission success. It also used a marker system for accurate autonomous operation near the asteroid [14].

Similarly, the *OSIRIS-REx* mission to asteroid 101955 Bennu also utilized human-in-the-loop OpNav during its approach, orbital phases, and sample collection. The spacecraft's onboard navigation system analyzed optical images captured by its navigation camera to determine its position relative to Bennu, particularly during its low-altitude maneuvers. This data allowed *OSIRIS-REx* to navigate Bennu's complex gravitational field, helping it to select sample collection sites and safely perform touch-and-go operations. The OpNav system provided real-time data during the mission's critical phases, including orbital insertion, detailed surface mapping, and final sample collection. Throughout the mission, OpNav proved invaluable in guiding the spacecraft during autonomous operations when Earth-based communication delays

are too long for manual intervention [15].

Existing OpNav methods have limitations that make them insufficient for autonomous spacecraft navigation. Natural feature tracking OpNav [15] is computationally expensive and may not be effective at large distances or near the dark side while using a physical marker method [14] requires close proximity to the asteroid for marker deployment. LOS [8] is advantageous due to its ease of use and applicability at large distances but at the cost of accuracy without range information. The newer silhouette methods [13] offer promising accuracy and determine asteroid poles and shapes in addition to localization but may be limited by computation time, except LimbNav [12] which is sufficiently computationally efficient for usage onboard spacecraft.

Another type of OpNav involves the horizon-based method. Unlike the other aforementioned methods, horizon-based OpNav measures the apparent horizon of the celestial body to determine the spacecraft's position and orientation, making it effective at a wide range of distances and lighting conditions [16]. Furthermore, it is computationally efficient and feasible for real-time autonomous applications. Horizon-based OpNav has yet to be fully utilized in asteroid missions, but its proven accuracy and reliability in spherical-body missions suggest it could be adapted to advance asteroid navigation capabilities. By using the asteroid's horizon rather than relying on surface features, horizon-based OpNav could ensure continuous and accurate navigation. It expands the range and angles at which measurements are sufficiently accurate to be usable and is effective from perspectives with low surface visibility, such as near the dark side. If successfully adapted for asteroid missions, it could help improve spacecraft autonomy, early mission approach time efficiencies, and reduce the need for manual interventions during critical mission phases. However, it is inaccurate when observing directly aligned with the lit or dark sides, as the horizon is detected erroneously or invisible.

Therefore, there is a need to develop a computationally efficient, autonomous, robust, and accurate OpNav and control algorithm. Ideally, this algorithm should function at a wide range of distances and angles while accounting for regions with poor observability to ensure continuous and safe operation. Various studies discuss robust orbit control around asteroids [17–24] but do not explicitly consider the navigation performance in their formulations. This research proposes a novel solution: developing a path-constrained Lyapunov controller that uses constraints to avoid poor optical observability during asteroid missions using the horizon-based method. Lyapunov control has been explored for application in the asteroid mission context, however the focus has been on orbit-attitude control and hovering operations [25–27]. This newly proposed controller is dedicated to improving the OpNav measurement method and ensuring that the spacecraft avoids regions with poor visibility by adjusting its trajectory in real-time. This approach allows for continuous and reliable optical measurements, even near the asteroid's dark side, thereby enhancing the overall safety and robustness of autonomous asteroid navigation.

There are existing techniques that enhance OpNav performance using different approaches than the one discussed in this paper. [28] introduces an approach to optimize the spacecraft’s orbit during the approach phase by enhancing OpNav observability using the Fisher Information Matrix (FIM). While this method significantly improves measurement reliability, it is still challenged by uncertainties due to the asteroid’s irregular surface and dynamic environment, which could introduce errors. Additionally, the optimization process is too time-consuming and computationally costly, thus posing a challenge for its onboard application. In another work [29], the authors develop data-driven image processing techniques for OpNav to enhance navigation accuracy around binary asteroids. However, the computational demand for processing large datasets in real-time presents a challenge, potentially limiting onboard resources. [30] presents an observability-based navigation strategy that combines optical and radiometric measurements to improve navigation during the asteroid approach phase. The spacecraft configuration is optimized to enhance measurement accuracy and state estimation. However, this is only applicable to multi-spacecraft formations.

The core technical approach of this paper involves deriving a Lyapunov controller that utilizes artificial potential functions to maintain a path with optimal observability. Additionally, we develop a synthetic asteroid image generation tool to simulate varying lighting conditions and test the performance of horizon-based OpNav in different scenarios. These simulations allow us to identify the limitations of existing OpNav methods, which then serve as inputs to our controller design. The proposed controller is tested in simplified mission scenarios, including orbit maintenance and approach for asteroid capture, with state estimation handled using an Extended Kalman Filter (EKF). The controller’s performance is evaluated using Monte Carlo simulations to ensure robustness across various mission profiles. A schematic displaying the flow of the algorithm is shown in Fig. 1

The remainder of this paper is structured as follows. First, we discuss the dynamics model, horizon-based OpNav, and EKF, which form the foundation of our navigation system. Next, we describe the asteroid image generation technique and the edge detection methods used to test OpNav and analyze its limitations. Following this, we present the novel contribution of the observability-constrained Lyapunov controller. Finally, we demonstrate the controller’s effectiveness by analyzing OpNav and EKF performance, validated using Monte Carlo simulations under simplified mission conditions.

2 Background and Preliminaries

2.1 Dynamics

The motion of a spacecraft near primitive celestial bodies, such as asteroids, is influenced by several forces, including the body’s gravitational pull and the Sun’s Solar Radiation Pressure (SRP). The equations governing this motion are encapsulated in the Augmented Normalized Hill Three-Body Problem (ANH3BP), which provides a

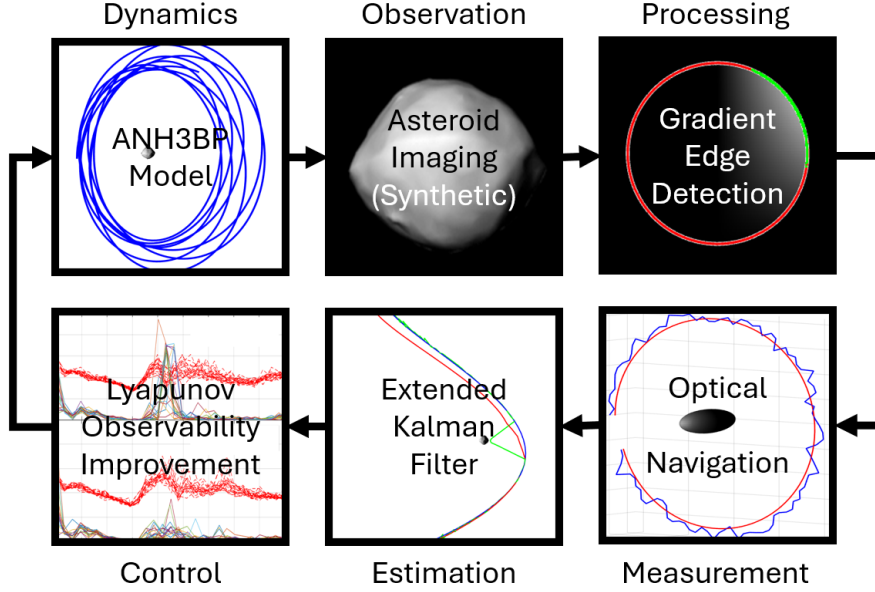


Fig. 1 Overall Algorithm Schematic

normalized framework accounting for these forces in a Cartesian rotating reference frame.

The Hill frame is defined with the x -axis pointing from the Sun to the asteroid, the z -axis pointing toward the angular velocity of the asteroid, and the y -axis completing the frame.

The spacecraft's normalized position and velocity are denoted by ${}^H\mathbf{r} = [x, y, z]^\top$ and ${}^H\mathbf{v} = [\dot{x}, \dot{y}, \dot{z}]^\top$ respectively within the Hill frame, where ${}^H\dot{\mathbf{r}}$ and ${}^H\dot{\mathbf{v}}$ are their time derivatives and the left superscript H represents that the vector is in the Hill frame. The dynamical system is non-dimensionalized with the unit length $(\mu/\mu_{\text{Sun}})^{1/3}R$ and unit time $1/N$ using the gravitational parameter of the primitive body μ and the Sun μ_{Sun} , the distance between the Sun and the primitive body R and the mean motion of the primary orbits, $N = \sqrt{\mu_{\text{Sun}}/R^3}$. The equations of motion for the ANH3BP are [31]:

$$\begin{aligned}\ddot{x} &= 2\dot{y} + 3x - x/\|{}^H\mathbf{r}\|^3 + \beta + u_x \\ \ddot{y} &= -2\dot{x} - y/\|{}^H\mathbf{r}\|^3 + u_y \\ \ddot{z} &= -z - z/\|{}^H\mathbf{r}\|^3 + u_z\end{aligned}\quad (1)$$

The non-dimensional acceleration due to SRP is represented by β and calculated as follows:

$$\beta = \left(\frac{G_1}{(m/A)R^2}\right) \left(\frac{1}{N}\right)^2 \left(\left(\frac{\mu}{\mu_{\text{Sun}}}\right)^{1/3} R\right)^{-1} = \frac{G_1}{(m/A)\mu_{\text{Sun}}^{2/3}\mu^{1/3}} \quad (2)$$

where G_1 is the solar flux constant and m/A is the spacecraft mass-to-area ratio. It is important to note that this model involves approximation due to the assumptions that the asteroid is in a circular orbit and SRP acceleration is constant.

An important defining condition for an orbit to be bounded around the primitive body within this model is the maximum semi-major axis, defined as follows [32]:

$$a_{\max} = \frac{\sqrt{3}}{4} \sqrt{\frac{\mu(m/A)}{G_1}} R \quad (3)$$

where a_{\max} is the maximum semi-major axis of the orbit beyond which escape occurs.

An alternate representation of these dynamics can be formulated using Milankovitch elements. First, let ${}^H \mathbf{x}_{\text{Milan}}$ be the state of our system in Milankovitch elements and express the equation of motion as follows:

$${}^H \dot{\mathbf{x}}_{\text{Milan}} = {}^H \mathbf{f}_0({}^H \mathbf{x}, t) + B {}^H \mathbf{u} \quad (4)$$

where ${}^H \mathbf{f}_0({}^H \mathbf{x}, t)$ represents the natural orbital dynamics and B is the control matrix that maps the control input ${}^H \mathbf{u}$ to the state.

To model the ANH3BP using Milankovitch elements, the Gauss planetary equations are used [33]. However, since Gauss planetary equations are conventionally represented in the inertial frame, ${}^H \mathbf{f}_0({}^H \mathbf{x}_{\text{Milan}}, t)$ must be modified accordingly. The rotation of the Hill frame relative to the inertial frame is considered using the transport theorem as follows:

$$\begin{aligned} {}^H \dot{\mathbf{h}} &= \dot{\mathbf{h}} - \tilde{\boldsymbol{\Omega}} \mathbf{h} = \tilde{\mathbf{r}} \mathbf{a}_d - \tilde{\boldsymbol{\Omega}} \mathbf{h} \\ {}^H \dot{\mathbf{e}} &= \dot{\mathbf{e}} - \tilde{\boldsymbol{\Omega}} \mathbf{e} = \frac{1}{\mu} (\tilde{\mathbf{v}} \tilde{\mathbf{r}} - \tilde{\mathbf{h}}) \mathbf{a}_d - \tilde{\boldsymbol{\Omega}} \mathbf{e} \end{aligned} \quad (5)$$

where the inertial rate of change of the angular momentum vector and eccentricity vector are $\dot{\mathbf{h}}$ and $\dot{\mathbf{e}}$ respectively. \mathbf{a}_d includes the perturbing accelerations of SRP, solar gravity and the control input. The rotation terms resolve to $-\tilde{\boldsymbol{\Omega}} \mathbf{h} = [-\Omega h_1, \Omega h_2, 0]^\top$ and $-\tilde{\boldsymbol{\Omega}} \mathbf{e} = [-\Omega e_1, \Omega e_2, 0]^\top$. $\mathbf{h} = \tilde{\mathbf{r}} \mathbf{v}$ is the angular momentum vector, \mathbf{e} is the eccentricity vector and the asteroid's angular momentum vector is $\boldsymbol{\Omega} = [0, 0, \Omega]$. The tilde operator notation is used on 3D vectors to create the cross product matrix in the following form:

$$\tilde{\mathbf{r}} = \begin{bmatrix} 0 & -r_3 & r_2 \\ r_3 & 0 & -r_1 \\ -r_2 & r_1 & 0 \end{bmatrix} \quad (6)$$

Additionally, the SRP and solar gravity perturbations are added by using the control influence matrix to map them from their Cartesian form to the Milankovitch form.

Therefore, the equations of motion in Milankovitch elements are as follows:

$$\begin{aligned}
{}^H \mathbf{f}_0({}^H \mathbf{x}_{\text{Milan}}, t) &= [-\Omega h_1, \Omega h_2, 0, -\Omega e_1, \Omega e_2, 0, \frac{h}{r^2}]^\top + B({}^H \mathbf{a}_{\text{SRP}} + {}^H \mathbf{a}_{\text{Solar}}) \\
{}^H \mathbf{x}_{\text{Milan}} &= [{}^H \mathbf{h}^\top, {}^H \mathbf{e}^\top, L]^\top \\
B &= \begin{bmatrix} {}^H \tilde{\mathbf{r}} \\ \frac{1}{\mu} ({}^H \tilde{\mathbf{v}} {}^H \tilde{\mathbf{r}} - {}^H \tilde{\mathbf{h}}) \\ \frac{{}^H \hat{\mathbf{z}} \cdot {}^H \mathbf{r}}{h(h + {}^H \hat{\mathbf{z}} \cdot {}^H \mathbf{h})} {}^H \mathbf{h} \end{bmatrix} \\
{}^H \mathbf{a}_{\text{SRP}} &= [\beta, 0, 0]^\top \\
{}^H \mathbf{a}_{\text{Solar}} &= -\mu \left(\frac{{}^H \mathbf{r}}{\|{}^H \mathbf{r}\|_2^3} + \frac{{}^H \mathbf{r}_{\text{asteroid}}}{\|{}^H \mathbf{r}_{\text{asteroid}}\|_2^3} \right)
\end{aligned} \tag{7}$$

where ${}^H \hat{\mathbf{z}}$ is the unit vector in the z-axis direction in the Hill frame, h is the angular momentum magnitude, h_1 and h_2 are the angular momentum components in the x and y directions, e_1 and e_2 are the eccentricity components in the x and y directions, and ${}^H \mathbf{r}_{\text{asteroid}} = [R, 0, 0]^\top$ in the Hill frame.

2.1.1 Frozen Terminator Orbit

The concept of a Frozen Terminator Orbit (FTO) is used as a preliminary test case throughout this work because it offers natural dynamical stability and good horizon-based observability conditions. The condition for an FTO is defined as follows [32]:

$$\frac{{}^H \mathbf{h}}{h} = \pm {}^H \hat{\mathbf{x}} \tag{8}$$

$$\frac{{}^H \mathbf{e}}{e} = {}^H \tilde{\mathbf{y}} \frac{{}^H \mathbf{h}}{h} \tag{9}$$

$$e = \cos \Lambda \tag{10}$$

where ${}^H \hat{\mathbf{x}}$ and ${}^H \hat{\mathbf{y}}$ are the unit vectors in the x and y directions in the Hill frame, while ${}^H \mathbf{e}$ represents the eccentricity vector and e its magnitude. Λ is an angle that indicates the relative strength of the SRP to parametrize the secular SRP dynamics. The result is a near-circular polar orbit with ${}^H \mathbf{h}$ aligned with the x-axis in the Hill frame and ${}^H \mathbf{e}$ is accordingly positioned above or below the ecliptic. This is a unique frozen orbit solution when considering SRP as the primary perturbation with a point mass small body gravity assumption. Any references to an FTO within the study will refer to this definition.

2.2 Horizon-based OpNav

The Christian-Robinson OpNav algorithm [16] and its analytical measurement covariance formulation [34] are utilized for the measurement implementation. It is an efficient and accurate computing method to calculate the position of an observer with respect to the center of mass of a target body as it directly computes from the

edge-detected horizon points rather than using curve fitting. The observations for the EKF and the simulation are derived from this OpNav process.

The inputs include the pixel coordinates of all the detected points in the camera frame, the inverse camera calibration matrix, the attitude transformation matrix between the parent body and the camera, and the triaxial parameters of the shape of the target body. The inverse camera matrix is defined as follows:

$$\mathbf{C}^{-1} = \begin{bmatrix} \frac{1}{d_x} & \frac{-\alpha}{d_x d_y} & \frac{\alpha v_p - d_y u_p}{d_x d_y} \\ 0 & \frac{1}{d_y} & \frac{-v_p}{d_y} \\ 0 & 0 & 1 \end{bmatrix} \quad (11)$$

where d_x and d_y are the unit pixel density in the x and y directions in the Hill frame, respectively, l is the focal length, $u_p = S/2$ and $v_p = S/2$ are the principal point coordinates, and α is the skew of the pixels. S is the image size measured in pixels. The focal length can be calculated as follows:

$$l = \frac{(S/2)}{\tan(\theta/2)} \quad (12)$$

where θ is the camera field of view angle.

The OpNav measurement returns values in the format

$${}^H \mathbf{z} = [r_{C,x}, r_{C,y}, r_{C,z}]^\top \quad (13)$$

where ${}^H \mathbf{r}_C$ is the relative position of the spacecraft to the center of mass of the target body in the spacecraft camera frame.

Since this is a case of known attitude, the magnitude of the position measurement returned by the OpNav algorithm is transformed into the ANH3BP coordinate frame using the current attitude.

2.3 Extended Kalman Filter

An Extended Kalman Filter (EKF) is used to perform the state estimation using the OpNav measurements. Testing the EKF's performance across various operational scenarios helps establish the algorithm's robustness and identify areas for enhancement. First, some key assumptions include the satellite's ability to continuously observe the asteroid with its optical camera via nadir pointing (i.e., the camera is always oriented to point towards the center of the target body), the attitude of the spacecraft relative to the Hill frame is always known, the asteroid shape is known, and the availability of initial state estimates with inherent uncertainties. These assumptions are made to simplify the problem and focus on estimating the position. Constraints involve the limitations of the camera's resolution and the accuracy of onboard sensors, the maximum

semi-major axis for a stable orbit in this system, and the computational complexity of generating and processing synthetic observation images in real time. The EKF algorithm used is as follows:

$$\begin{aligned}
\hat{\mathbf{x}}_{k|k-1} &= f(\hat{\mathbf{x}}_{k-1|k-1}, \mathbf{u}_{k-1}) \\
\mathbf{P}_{k|k-1} &= \mathbf{F}_k \mathbf{P}_{k-1|k-1} \mathbf{F}_k^\top + \mathbf{Q}_{k-1} \\
\tilde{\mathbf{y}}_k &= \mathbf{z}_k - h(\hat{\mathbf{x}}_{k|k-1}) \\
\mathbf{S}_k &= \mathbf{H}_k \mathbf{P}_{k|k-1} \mathbf{H}_k^\top + \mathbf{R}_k \\
\mathbf{G}_k &= \mathbf{P}_{k|k-1} \mathbf{H}_k^\top \mathbf{S}_k^{-1} \\
\hat{\mathbf{x}}_{k|k} &= \hat{\mathbf{x}}_{k|k-1} + \mathbf{G}_k \tilde{\mathbf{y}}_k \\
\mathbf{P}_{k|k} &= (\mathbf{I} - \mathbf{G}_k \mathbf{H}_k) \mathbf{P}_{k|k-1}
\end{aligned} \tag{14}$$

where f is the non-linear state transition function, the state transition matrix \mathbf{F} is calculated as the Jacobian of the equations of motion of the ANH3BP from Equation 1 and the observation matrix \mathbf{H} is $[\mathbf{I}_{3 \times 3}, \mathbf{0}_{3 \times 3}]^\top$.

2.4 Lyapunov Control

Lyapunov control is a method that ensures dynamical system stability by developing Lyapunov functions in a nonlinear feedback control case. It is beneficial as it allows for creating an analytical controller with light computational cost and is easy to implement. Furthermore, it is possible to incorporate path constraints using artificial penalty functions. However, the Lyapunov controller does not guarantee satisfaction of the path constraint and requires parameter tuning. It may also not return an optimal solution, but its efficiency and satisfactory performance prove it to be a good option for this research. A Lyapunov function [35] is a scalar continuous function $V(\mathbf{x})$ that is locally positive definite about a reference state \mathbf{x}_r of an autonomous system $\dot{\mathbf{x}} = \mathbf{f}(\mathbf{x})$.

In spacecraft control, Lyapunov functions can be designed to guide the spacecraft's state toward a desired configuration, such as a stable orbit, attitude, or particular rendezvous point [36]. By defining an appropriate Lyapunov function for a spacecraft's position and velocity, the system can be controlled to remain stable under perturbations, such as SRP or irregular gravitation in the case of an asteroid. control inputs are applied to approach a desired target state. These inputs are derived from the gradient of the Lyapunov function, ensuring that the spacecraft moves in a direction that reduces the overall system energy. The approach is to design a controller $\mathbf{u} = \mathbf{c}(\mathbf{x})$ such that $V(\mathbf{x})$ is a Lyapunov function.

3 Synthetic Image Generation Pipeline

The image generation is done using built-in Matlab graphics tools. The procedure involved illuminating a white sphere, ellipsoid, or 3-dimensional mesh model of an asteroid against a black background with the mean radius of Bennu (or any sample

asteroid) using an infinitely far away light source that is aligned to originate from the negative x -axis in the Hill frame to represent a parallel ray light source like the Sun. The camera is then placed based on an input distance, azimuth, and elevation calculated from the current spacecraft position and an image is captured. Gaussian white noise is added to the image to add realistic complexity for the filter to process. Edge detection is executed by identifying high gradient magnitudes between pixels on the image, which is commonly where the lit limb edge meets blank space. The generated images were compared with those produced by existing higher fidelity image generators in identical conditions and found to be sufficiently accurate when comparing the resulting OpNav measurement. Below is a stepwise summary of the process utilized for the synthetic image generation:

1. Generate a sphere, ellipsoid, or mesh scaled according to the camera settings and distance or an experimentally determined scale factor. A fixed scale factor of 1.3065 was experimentally found to produce the best OpNav performance with minimal measurement bias to adjust according to the inherent scaling bias encountered when generating images using the MATLAB figure environment. This was found by visually comparing generated images with real images and verifying the OpNav measurement across a range of distances, then fitting a scale factor based on the linear relationship between error and distance.
2. Rotate the object using a specified axis and angle. In the context of this paper, Bennu’s retrograde rotation properties are used. The axis is at approximately 180° [37] from the z -axis in the Hill frame with a synodic rotation period of 4.296057 hours [38]. This information is used to calculate and apply the angle by which the object had rotated at each time step during simulation with the equation $\theta_{\text{asteroid}} = \frac{t}{t_{\text{rp}}} 360^\circ$ where θ_{asteroid} is the angle by which the asteroid has rotated, t is the time elapsed and t_{rp} is the asteroid’s synodic rotation period.
3. Create a figure with invisible, equal, tight axes and a black background. Plot the generated object as a surface with `LineStyle` set to none and a white colormap.
4. Set the view angle, camera position, and roll according to the current spacecraft attitude.
5. Delete existing lights and replace them with a light set at an infinite distance to simulate the Sun. Use Gouraud lighting and dull material for realistic surface and lighting conditions, with no ambient or specular reflection, a diffused reflection coefficient of 1, and a shininess coefficient of 10. These parameters were chosen as they produced the most visually accurate images compared to real examples.
6. Set the figure size and axis limits according to the image size, apply the camera’s FOV setting to the axes’ camera view angle, and set aspect ratios to be equal
7. Store the image as a frame, then convert it to an image and resize it to the calculated image size in pixels. Convert the image to grayscale and output it for further processing.

The synthetic image generation process is also expressed in Algorithm 1:

Algorithm 1 Asteroid Image Generation Procedure

1: **procedure** *img*=IMAGEGENERATOR(*x_y_z*, *up*, *dist*, *FOV*, *imgSize*, *rad*, *ellip_shape*, *R_ellip*)

Input:

x_y_z: Camera direction vector

up: Camera "up" pointing direction vector

dist: Distance from camera to object center

FOV: Camera field of view

imgSize: Desired square image dimension in pixels

rad: Characteristic radius of the asteroid

ellip_shape: Scaling factors (*a*, *b*, *c*) matrix defining ellipsoid shape

R_ellip: Rotation angle about the chosen rotation axis

R_axis: Rotation axis vector in body frame

Output:

A grayscale image of the half-illuminated ellipsoid approximating the asteroid.

- 2: Generate object (sphere, ellipsoid or mesh) [*X*, *Y*, *Z*] coordinates using center=(0, 0, 0) and shape=*ellip_shape*
 - 3: Scale object by a scale factor of 1.3065
 - 4: Rotate Object by axis=*R_axis* and angle=*R_ellip*
 - 5: Create a figure with a black background and invisible, equal, and tight axes
 - 6: Plot object with invisible edges and white color
 - 7: Set viewDirection=*x_y_z*
 - 8: Set cameraPositionNormalize=*dist* · *x_y_z*
 - 9: Set cameraUpDirection=*up*
 - 10: Set light at infinite distance with direction=[-100] and Gouraud type
 - 11: Set dull material with 0 ambient and specular, full diffuse reflectivity and shininess coefficient of 10
 - 12: Set figure size = *imgSize* and axis limits = [-*imgSize*/2, *imgSize*/2]
 - 13: Apply camera field of view = *FOV*
 - 14: Convert image to grayscale
 - 15: Apply noise to the image
 - 16: Return the image
 - 17: **end procedure**
-

A few examples of generated images are shown in Fig. 2

A gradient-based approach detects the horizon points from the generated synthetic images. First, calculate the gradient of the image matrix and find the gradient magnitude at each pixel. Next, find the maximum gradient magnitude across the entire image. Then, multiply this value by 0.7 to define a minimum gradient threshold and find the pixel coordinates of all points with a gradient magnitude above it. These are the desired horizon points. The value of 0.7 was chosen for the best performance after some experimental testing. To avoid detecting random noisy pixels, the absolute minimum gradient threshold was set to 0.1, which was determined experimentally by finding an appropriate threshold above the maximum gradient in dark-side lighting

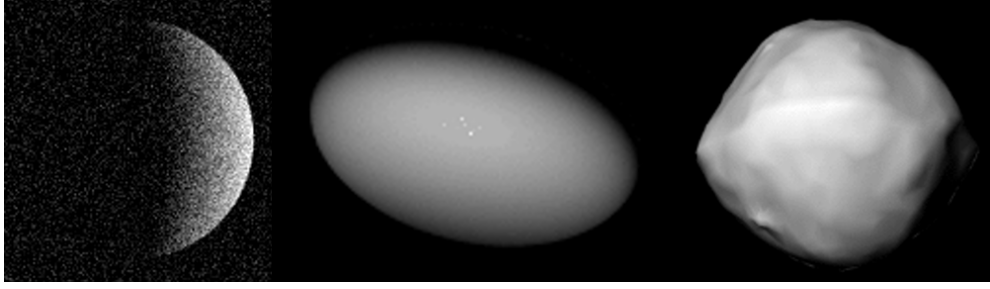


Fig. 2 Example synthetic images of a half-illuminated sphere with noise (left), ellipsoid (center), and Bennu model at a distance of 5 radii (right)

conditions but below the maximum gradient of regular lighting conditions. The edge detection process is expressed in Algorithm 2:

Algorithm 2 Gradient Edge Detection Procedure

procedure $points = \text{GRADIENTEDGEDETECT}(img, threshold)$

Input:

img : A grayscale image of the half-illuminated ellipsoid approximating the asteroid.

$threshold$: The gradient threshold used to determine edge points.

Output:

$points$: A $3 \times n$ matrix containing the coordinates of the lit edge pixels detected with each pixel stored in the form $[x, y, 1]^T$

- 2: Convert img to numerical double format (img_dbl) for gradient calculation
Calculate the 2D $gradient$ of img_dbl
 - 4: Compute the $gradient_magnitude$ from the $gradient$
Calculate $minimum_gradient = threshold \times MAX(gradient_magnitude)$
 - 6: Add all points with $gradient_magnitude > minimum_gradient$ to $points$
Return $points$
 - 8: **end procedure**
-

4 Observability-constrained Controller Design

The goal is to design a controller that generates a controlled trajectory along which the view of the asteroid is always in favorable lighting conditions. The objective is to develop a Lyapunov controller that avoids certain regions where the OpNav algorithm performs poorly. These poor observability regions have been characterized experimentally in Section 5.

4.1 Path Constraint Formulation

The path constraints have been experimentally determined by testing the OpNav algorithm's performance across varying distances and angles.

The constraints are listed as follows:

1. Minimum radius constraint: $R_{\min} - \|\mathbf{r}\|_2 \leq 0$ with $R_{\min} = 2R_{\text{asteroid}}$
2. Maximum radius constraint: $\|\mathbf{r}\|_2 - R_{\max} \leq 0$ with $R_{\max} = 25R_{\text{asteroid}}$
3. Keep-out Cone: $\frac{y^2+z^2}{x^2} - \tan^2 \alpha \leq 0$ with $\alpha = 30^\circ$

where R_{asteroid} is the radius of the asteroid.

Now, we define our three penalty constraints in mathematical terms applicable to either controller. Start by deriving the minimum radius constraint using the parameter r_{\min} :

$$g_1(\mathbf{x}) = r_{\min}^2 - \|\mathbf{r}\|_2^2 = r_{\min}^2 - \frac{h^2/\mu}{1+e} \quad (15)$$

Repeat the process for the maximum radius constraint r_{\max} .

$$g_2(\mathbf{x}) = \|\mathbf{r}\|_2^2 - r_{\max}^2 = \frac{h^2/\mu}{1+e} - r_{\max}^2 \quad (16)$$

Repeat the process for the cone constraint along x -axis with half angle α .

$$g_3(\mathbf{x}) = \cos\left(\frac{\pi}{2} + \alpha\right) - \left(\frac{h_1}{h}\right) \quad (17)$$

h_1 is the component of angular momentum in the x -axis direction in the Hill frame. The partial derivatives of the path constraints are computed in Section A

4.2 Controller Derivation

Milankovitch elements are used for the controller because they have no singularity and can target a certain orbit state over a specific point. We start by only targeting the slow variables and freeing the fast variable, which in this case would be the true longitude. Although the rotation between the Hill and inertial frames was found to affect the angular momentum and eccentricity vector components of \mathbf{f}_0 in Section 2.1, it is possible to assume $\mathbf{f}_{0,slow} \approx 0$. Therefore, ${}^H\dot{\mathbf{x}}_{slow} = B_{slow}{}^H\mathbf{u}$. This assumption is reasonable because the orbital angular velocity of Bennu is approximately $(360/436.649) = 0.824[\text{degrees/day}]$ or $1.665 \times 10^{-7}[\text{rad/s}]$ which only leads to a total rotation of about 5 degrees over the duration of the simulations in this research, which is at most 6 days long. For reference, 436.649 days is the orbital period of Bennu [38]. However, this assumption is only applied for the controller derivation and only affects the theoretical stability guarantees in the context of Lyapunov control. Numerical

dynamics propagations are based on the true dynamics. Thus, the error state can be defined as follows:

$$\delta^H \mathbf{x}_{\text{slow}} = {}^H \mathbf{x}_{\text{slow}} - {}^H \mathbf{x}_{\text{slow}}^* \quad (18)$$

where the slow state can be written as follows:

$${}^H \mathbf{x}_{\text{slow}} = [{}^H \mathbf{h}^\top, {}^H \mathbf{e}^\top]^\top \quad (19)$$

Next, considering a candidate Lyapunov function as follows:

$$V = \delta^H \mathbf{x}_{\text{slow}}^\top K \delta^H \mathbf{x}_{\text{slow}} \quad (20)$$

where $K \in \mathbb{R}^{6 \times 6}$ and is positive definite. Therefore, the Lyapunov rate is:

$$\dot{V} = 2\delta^H \mathbf{x}_{\text{slow}}^\top K \delta^H \dot{\mathbf{x}}_{\text{slow}} \quad (21)$$

The next step is to incorporate path constraints using artificial potential functions. To do this, the Lyapunov function and rate results need to be augmented by considering some additive potential function V_{P_i} from each penalty function, which we can define in the following form:

$$V_P = wV({}^H \mathbf{x})P(g({}^H \mathbf{x})) \quad (22)$$

where w is the weight of the penalty, and P is the penalty function in terms of the path constraint $g({}^H \mathbf{x}) \leq 0$, which must be negative at the target state and smooth everywhere. The penalty function should also monotonically increase in g for $g > 0$. For this, we define the penalty functions as set to 0 when the constraint condition is not violated and greater than 0 when it is. This can be represented as follows:

$$P(g) \begin{cases} > 0 & g > -\epsilon \\ = 0 & g \leq -\epsilon \end{cases} \quad (23)$$

where ϵ may be defined to represent the point at which the constraint becomes applicable. We use the exponential form for all of our constraints since it is a smooth and continuous function and, therefore, compatible with the Lyapunov context.

$$P_i(g_i) = e^{k_i g_i} \quad (24)$$

where $i = 1, 2, 3$ represents the corresponding path constraint and k is the sharpness parameter, one of the variables that may be tuned. Now, we may add the three desired artificial potentials for each path constraint penalty as follows:

$$\hat{V} = V + V_{P_1} + V_{P_2} + V_{P_3} \quad (25)$$

Substituting in for the weights and penalty functions and then taking the derivative, we find the augmented Lyapunov rate expression:

$$\dot{V} = \dot{V}(1 + \sum \omega_i P_i) + V \sum \omega_i \dot{P}_i \quad (26)$$

Use the following chain rule properties to compute the derivatives of V and P_i :

$$\dot{V} = \frac{dV}{d^H \mathbf{x}_{\text{slow}}} \frac{d^H \mathbf{x}_{\text{slow}}}{dt} = (\delta^H \mathbf{x}_{\text{slow}}^\top K) B_{\text{slow}}^H \mathbf{u} \quad (27)$$

$$\dot{P}_i = \frac{dP_i}{dg_i} \frac{dg_i}{d^H \mathbf{x}} \frac{d^H \mathbf{x}}{dt} = \frac{dP_i}{dg_i} \frac{dg_i}{d^H \mathbf{x}} + B_{\text{slow}}^H \mathbf{u} \quad (28)$$

Additionally, to get the desired stabilizing controller, we then set the Lyapunov rate equal to a negative definite quadratic form and algebraically solve for the control expression.

$$\delta^H \mathbf{x}_{\text{slow}}^\top (2(1 + \sum \omega_i \dot{P}_i) K + (K \delta^H \mathbf{x}_{\text{slow}}) \sum \omega_i \frac{dP_i}{dg_i} \frac{dg_i}{d^H \mathbf{x}_{\text{slow}}}) B_{\text{slow}} \mathbf{u} = -\delta^H \mathbf{x}_{\text{slow}}^\top I_{6 \times 6} \delta^H \mathbf{x}_{\text{slow}} \quad (29)$$

For compact expression, define the following:

$$L = (2(1 + \sum \omega_i \dot{P}_i) K + (K \delta^H \mathbf{x}_{\text{slow}}) \sum \omega_i \frac{dP_i}{dg_i} \frac{dg_i}{d^H \mathbf{x}_{\text{slow}}}) B_{\text{slow}} \quad (30)$$

where $L \in \mathbb{R}^{6 \times 3}$ and assumed to be full rank. Lastly, Solve for the control ${}^H \mathbf{u}$ by using a pseudo-inverse since L is not square:

$${}^H \mathbf{u} = -(L^\top L)^{-1} L^\top \delta^H \mathbf{x}_{\text{slow}} \quad (31)$$

5 OpNav and EKF Performance Analysis

To start, a simplified base case is used by choosing the asteroid Bennu for which abundant information is available [2, 39]. This is ideal for testing and tuning the filter as simulated 'truth' and filter predictions can be validated. The relevant initial conditions and properties used are shown in Table 1, where M is the asteroid's mass, e is the eccentricity of the asteroid's orbit, and r is the mean radius of the asteroid. Additionally, the OpNav parameters used for this research are shown in Table 2.

5.1 Distance and Angle Accuracy Analysis

The OpNav algorithm's accuracy at varying distances and lighting conditions is examined by running multiple simulations with noise at varied fixed points.

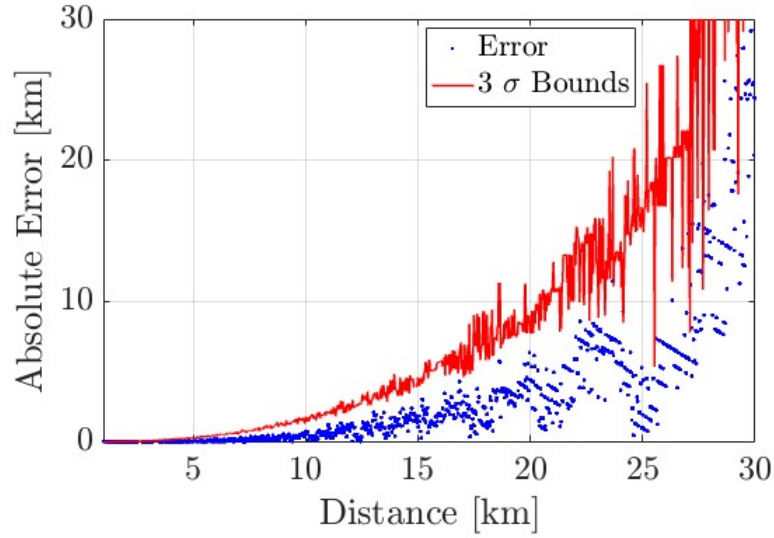
Table 1 Dynamical Parameters

Parameter	Value
M	7.329×10^{11} kg
μ	4.890×10^{-9} km ³ /s ²
μ_{Sun}	1.327×10^{11} km ³ /s ²
G_1	1×10^8 kg.km ³ /(s ² .m ²)
B	33
a	1.685×10^8 km
e	0.204
d	1.720×10^8 km
r	0.241 km

Table 2 OpNav Parameters

Parameter	Value
θ_{FOV}	90°
S	1000 pixels
α	0
dx	1
dy	1

In the case of distance, 1000 test cases are run starting from a distance of 1 km up to 30 km. A side-on view where exactly half of the body is lit is used for consistency to fix the angle at a value where the OpNav algorithm is known to be accurate. As can

**Fig. 3** Plot of the OpNav Measurement Error Variation over Distance with Error Magnitude (blue points) and Analytical Covariance (red line)

be seen in Fig. 3, the OpNav algorithm is highly effective at low range but starts to

involve major error at distances greater than 25-30 times the radius of the asteroid. In this case, we can see that deviation becomes visibly significant after a distance of around 10 km. However, the analytical covariance still provides a good envelope for the errors. We can define one range observability constraint based on this result. While OpNav still provides results beyond this, eventually, the magnitude of the error exceeds the absolute value of the distance itself, making it unusable after a certain point. Therefore, the algorithm must be used within this range, which has now been successfully determined. This distance is still a greater capability than near-range observation methods, which require the spacecraft to be much closer than 25-30 times the asteroid's radius.

In the case of lighting conditions, 1000 test cases are run starting from -90 degrees (straight-on or full moon) up to +90 degrees (dark-side or new moon), where 0 degrees is aligned with the side-on view. These are done with a fixed distance of 5 km for consistency and at a range where the OpNav algorithm is accurate.

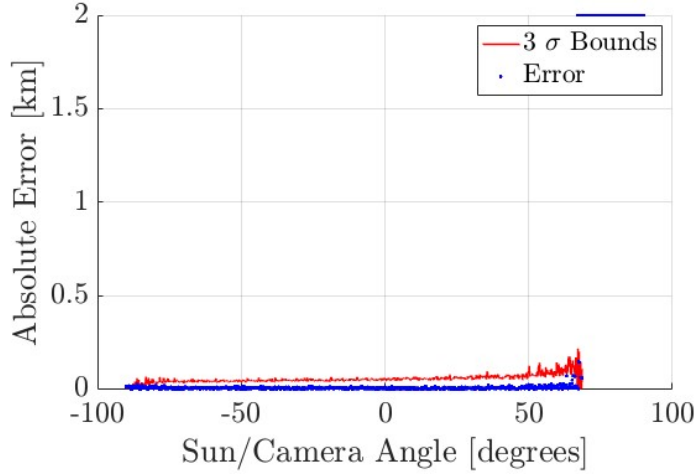


Fig. 4 Plot of the OpNav Measurement Error Variation over Angle with Error Magnitude (blue points) and Analytical Covariance (red dashed line)

We can infer from Fig. 4 that the algorithm is accurate for most angles except straight-on due to the terminator effect and angles close to the dark side as the size of the lit horizon shrinks. The performance deteriorates if the spacecraft views the asteroid from within 30 degrees of the $+x$ axis near the dark side. The covariance is undefined when viewing the dark side, as no horizon points are detected. The error is accordingly equivalent to the true distance of the spacecraft in the implementation used for this research, as the OpNav algorithm returns a zero measurement due to an absence of input horizon points. In other words, the measurement is unusable in these lighting conditions. From this experiment, we define a keep-out cone to ensure

observability, which is given as a cone with a 30-degree half-angle along the positive x -axis.

5.2 Elliptic Shape Performance

We now test the OpNav performance against increasingly elliptical bodies. The shape ratios are represented using the notation $[a,b,c]$ where a , b and c represent the principal axis dimensions of the triaxial ellipsoid body and the principal axis frame is defined such that $a \geq b \geq c$ according to convention [16]. To isolate the effect of body ellipticity, rotation is ignored for this test. As can be seen in Fig. 5, the OpNav error and covariance increase with highly elliptical bodies. The error is correctly bounded by the covariance for all cases up to an ellipsoid with a shape ratio of $[5,1,1]$, supporting its usability for state estimation with ellipsoid bodies. For this test case, we simulate along one revolution of an FTO with a radius of 2.0429km.

5.3 Rotating Ellipsoid Performance

The elliptic shape scenario is repeated with rotation to determine its effect on OpNav performance. A $[2.5,1,1]$ ellipsoid with the rotation period and axis of Bennu as described in Section 3 is used. For this test case, we simulate along one revolution of an FTO with a radius of 2.0429km. The result suggests that rotation significantly impacts the accuracy of OpNav, likely due to various alignments leading to lit limb geometries that are better or worse for accuracy. While the measurement error was found to be correctly bounded in the non-rotating $[5,1,1]$ ellipsoid test case, the $[2.5,1,1]$ ellipsoid seems to be near the limit of usability when considering rotating bodies. The error is marginally bounded by the covariance in this case and the error magnitude is significant.

5.4 Edge Detection Threshold Analysis

This implementation uses a pixel gradient method to detect the asteroid's lit limb edge. The maximum gradient on the image is found. All pixels with a gradient within a certain threshold of the maximum gradient are stored as the detected edge points for the OpNav measurement. The selection of this gradient, a value between 0 and 1, is critical to the measurement performance. Thus, we analyzed the performance for varying thresholds. The difference between the limb detected by a high threshold and the ideal threshold is shown in Fig. 7. Lower thresholds were found to lead to a higher lit limb angle and number of detected points, coupled with a lower analytical covariance. Using a lower threshold may also increase the risk of misdetecting background noise or excess points (such as those along the terminator line) leading to inconsistencies between the analytical and measurement covariance. The opposite effect holds for higher thresholds. Its error did not exceed the measurement covariance as lower thresholds may have due to detecting an excess number of points or including background noise. The ideal balance was found to be a value of 0.4 as it had consistently improved performance from higher thresholds, particularly for ellipsoid cases. At this threshold, sufficient points are included to characterize the asteroid silhouette, while

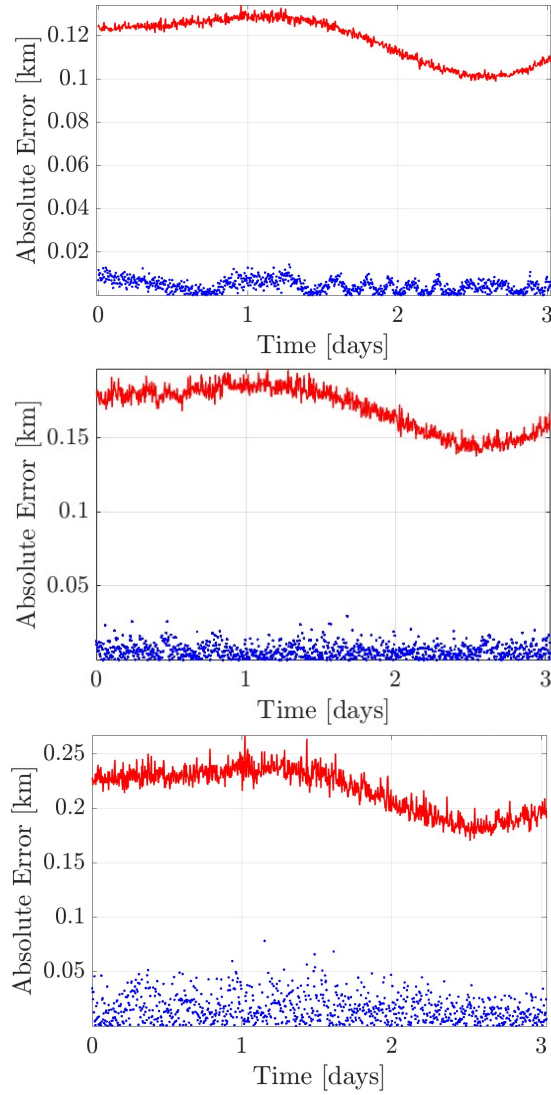


Fig. 5 OpNav Measurement Error Plots for Sphere (top), $[3,1,1]$ (center) and $[5,1,1]$ (bottom) Ellipsoid with Error Magnitude (blue points) and Analytical Covariance (red line) over time

avoiding inconsistencies in analytical and measured covariances or detecting erroneous points.

5.5 Trajectory Testing

The OpNav algorithm and EKF are tested across various types of trajectories, such as hyperbolic approaches and flybys, distant encirclements, and more, to ascertain properties of its performance across various situations and deduce when it is more effective or may have room for further improvement.

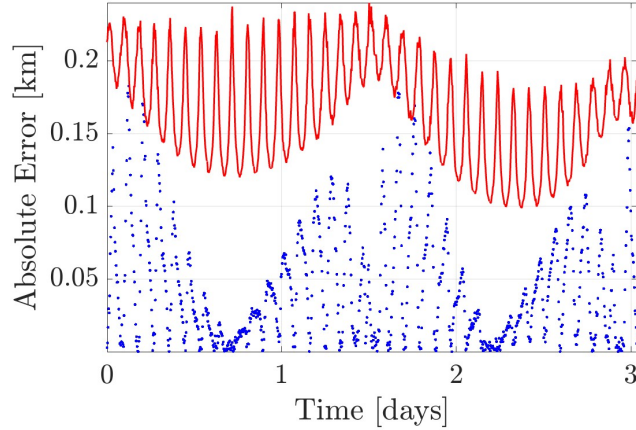


Fig. 6 OpNav measurement error (blue points) and analytical covariance (red line) over time for a rotating $[2.5, 1, 1]$ ellipsoid

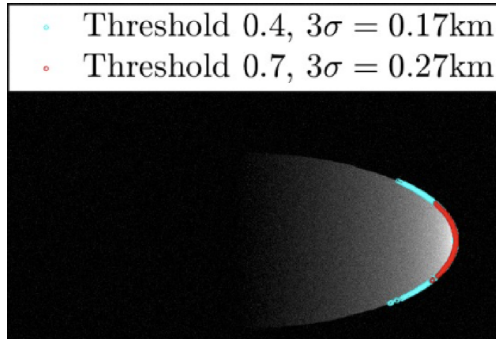


Fig. 7 Example of detected limbs for edge detection thresholds of 0.4 (longer cyan arc) and 0.7 (shorter red arc) with 3σ values of the error in position measurement norm

These initial conditions are arbitrarily chosen in terms of both position and velocity to provide some variation and generate natural paths that a spacecraft may follow depending upon its nature of approach to an asteroid. A few sample results are in Fig. 8. The first case depicted a hyperbolic flyby from a large distance. The second test is conducted at a medium range, keeping a similar distance from the asteroid while changing the lighting condition. The last case demonstrates another flyby where the asteroid is approached closely, and the spacecraft passes through the dark side.

Based on the behavior in Fig. 8, we can infer that position estimation is best when approaching near-linearly from the same angle or in close proximity to the asteroid. Horizon-based OpNav, and hence EKF, become inaccurate when the angle varies extremely in a short time or has a highly nonlinear trajectory as seen in the divergence of the OpNav measurements in each test case. Horizon-based OpNav performs

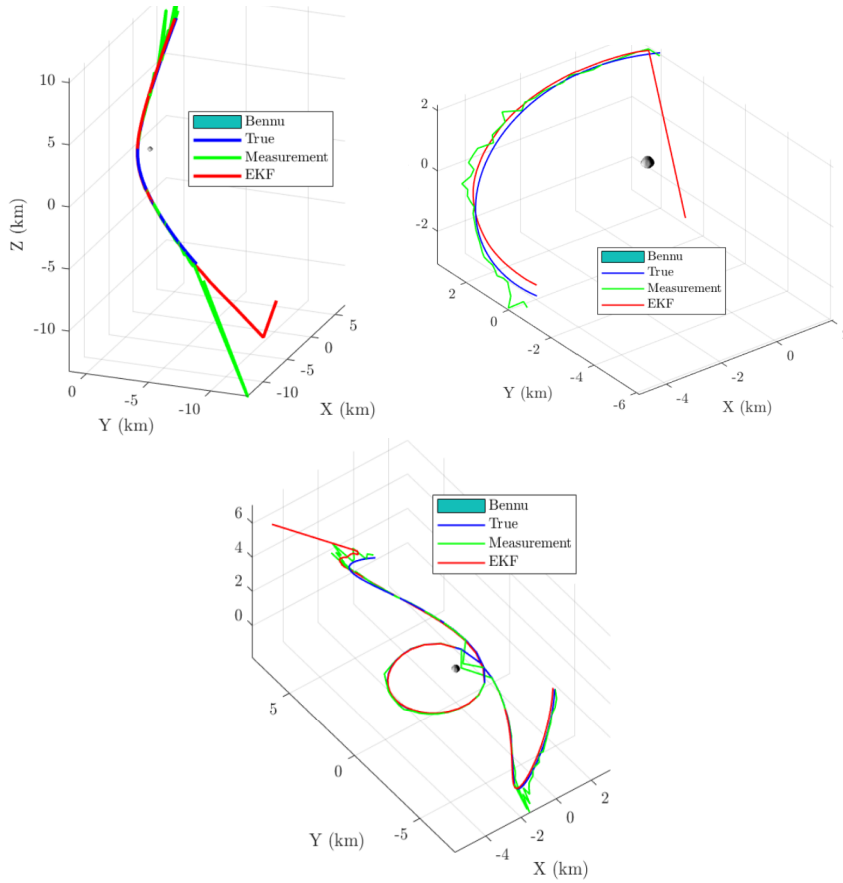


Fig. 8 Sample OpNav Testing Trajectories with a hyperbolic approach (top left), distant flyby (top right) and single revolution close proximity flyby (bottom)

well within medium range when in a hyperbolic approach trajectory before the view angle starts changing rapidly (before/after the viewpoint).

6 Numerical Results

To simulate the application of the Lyapunov controller in a simplified scenario, we implemented it in a loop such that the Lyapunov controller computes each successive timestep based on the EKF's prediction rather than using the true position. The true state is then updated using the control calculated by the controller, from which the OpNav measurement is taken at a realistic frequency of every 1.5 hours and provided to the EKF for the next prediction. This means that any significant error in the EKF's position estimate for the spacecraft could lead to a complete divergence of the true and estimated states.

Following is a table that summarizes all the relevant penalty weights for both scenarios: The penalty weight parameter subscript indicates the corresponding path

Table 3 Penalty Weight Parameters

Parameter	Value
ω_1	1
k_1	1
ω_2	1
k_2	1
$\omega_{3,1}$	10
$\omega_{3,2}$	100
k_3	1

constraint the parameter is relevant to according to the definitions in Section 4.1. All parameters have identical values except the cone weight, for which $\omega_{3,1}$ is used for the Asteroid Approach Targeting controller and $\omega_{3,2}$ is used for the Orbit Transfer controller.

6.1 Orbit Maintenance Scenario

To demonstrate the effectiveness of the observability-constrained controller, we develop a test scenario where a spacecraft starts with an arbitrary initial condition on a trajectory to flyby passing behind the dark side of Bennu. The target is a circular orbit with an inclination just above 30 degrees. This avoids the dark-side cone but provides a useful edge case to test where the spacecraft may often travel through the poor observability region in its controlled trajectory without an observability penalty. The initial conditions in cartesian terms are ${}^H\mathbf{r} = [1.0214, 0, -2.0429]^\top$ km and ${}^H\mathbf{v} = [40.493, 40.493, 40.493]^\top$ mm/s. The gain found to provide the best performance in terms of stability and rate of convergence is as follows:

$$K_2 = \text{diag}(10^{-2}, 10^{-3}, 10^{-3}, 10^{-4}, 10^{-3}, 10^{-4}) \quad (32)$$

For this case, the following initial covariance is used (covariances for the position in $[\text{km}^2]$ and velocity in $[\frac{\text{km}^2}{\text{s}^2}]$):

$$P_0 = \text{diag}(3.2761, 3.2761, 3.2761, 8.544 \times 10^{-17}, 8.544 \times 10^{-17}, 8.544 \times 10^{-17}) \quad (33)$$

To compare results, we test the Lyapunov controller without the observability improving penalty functions as shown in Fig. 9. The figure depicts the spacecraft's true trajectory, OpNav measurement, EKF position estimate and a visualization of the keep-out cone. As can be seen in the results for the controller without an observability penalty, the spacecraft travels through the poor observability region near the asteroid's dark side. This leads to a faulty measurement characterized by the spike in the OpNav measurement history, which causes the true and EKF-estimated trajectories to diverge.

We now compare this performance to that of the observability-constrained controller in Fig. 10. In the observability-constrained case, the controller successfully avoids the poor observability region, as can be seen by consistently matching the OpNav measurement and EKF prediction to the true trajectory at all times. An additional test was executed with a $[2.5 \ 1 \ 1]$ ellipsoid using the rotation parameters of Bennu and an approximation from its known mean radius.

Camera snapshots of each case with the detected horizon points highlighted in red can be seen in Fig. 11. It displays the image history from the spacecraft camera perspective and allows us to make physical inferences about the controller’s performance. For the leftmost case without the observability-constrained control, the spacecraft does not avoid the keep-out cone which causes the lit limb to go out of view in the fourth and fifth images. Thus, the number of detected horizon points significantly decreases, causing the spacecraft to diverge. The limb comes back into view later, but is at a larger distance due to the divergence, making the measurement less effective. The middle case displays the same example but with the observability-constrained control, with which we see that the lit limb is kept within view throughout the trajectory. The rightmost case displays the view of the $[2.5 \ 1 \ 1]$ ellipsoid using observability-constrained control to demonstrate the controller’s consistency in performance across varying shapes of celestial bodies. Although the size of the lit limb varies considerably due to the body’s rotation and viewing the ellipsoidal geometry from different angles, it maintains the lit limb within view by avoiding the poor observability zone and therefore produces more reliable measurements. Both the middle and rightmost cases avoid the divergence and disappearance of lit limb encountered in the leftmost case, supporting the benefit of the observability-constrained controller.

The maximum fuel consumption to execute the control used during this trajectory was calculated to be approximately 0.2 kg over 3 days, which is a reasonable quantity within its fuel reserves. The properties of the OSIRIS-REx spacecraft used were an ISP of 230 seconds and a spacecraft mass of 2110 kg [38]. The equation used was $\Delta m = m_{sc} \cdot \sum (u_{vec}) \cdot \Delta t \cdot \frac{1}{I_{sp} \cdot g_0}$ where $m_{sc} = 2110 \text{ kg}$ is the spacecraft mass, u_{vec} is the total acceleration imparted (in m/s^2), Δt is the time step, $I_{sp} = 230 \text{ s}$ is the specific impulse, and $g_0 = 9.80665 \text{ m/s}^2$ is the standard acceleration due to gravity.

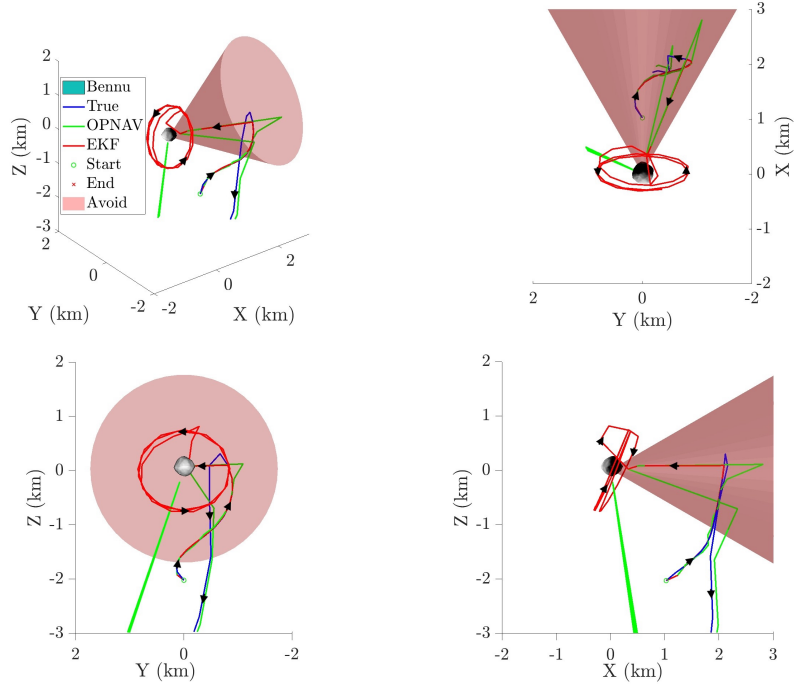


Fig. 9 True (blue), OpNav measurement (green), EKF-estimated (red) Trajectories and keep-out cone (shaded red) without Observability-constrained Penalty Lyapunov control around Benu shown in 4 views. Initial position (green circle), final position (red cross) and orbital direction (black arrows) indicated.

6.1.1 Monte Carlo Analysis

To demonstrate the algorithm's robustness, a Monte Carlo analysis is conducted to analyze its success rate statistically. A realistic initial standard deviation is defined for the position error across each direction (x, y and z in the Hill frame) of $\sigma = 30$ meters, approximately 10% of Benu's radius. This is used to apply an initial error to the true initial state to generate the EKF's initial known state. The Monte Carlo is run for 200 iterations. To start, we test the version without observability constraints to understand the severity of failures in this scenario. As per the results, the Lyapunov controller fails in almost every case without the observability constraint, as it passes through the poor observability region in every test. It succeeds in 8 out of 200 iterations for a success rate of 4%. The EKF and true dynamics diverge completely and lead to the spacecraft either crashing into the asteroid or traveling out of the system. Now, we compare this with the observability-constrained case. The observability-constrained Lyapunov controller shows better performance and success rate of the spacecraft reaching its desired orbit. It succeeds in 196 out of 200 iterations for a success rate of 98%. This is a major performance improvement and supports the utility of the observability-constrained controller. The ellipsoid case succeeds 161

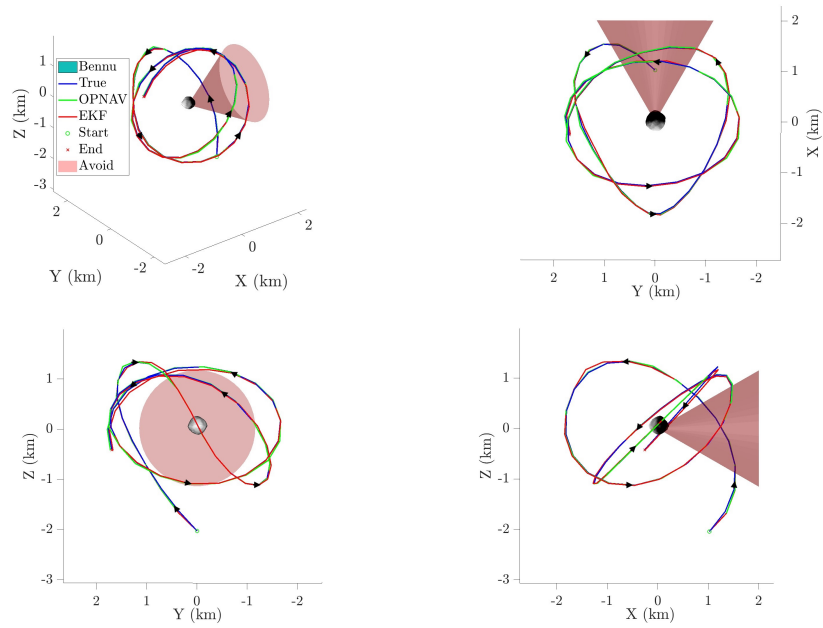


Fig. 10 True (blue), OpNav measurement (green), EKF-estimated (red) Trajectories and keep-out cone (shaded red) with Observability-constrained Penalty Lyapunov control around Benu shown in 4 views. Initial position (green circle), final position (red cross) and orbital direction (black arrows) indicated.

out of 200 iterations for a success rate of 80.5%. The performance degrades with non-spherical objects but maintains an improvement over the case without an observability constraint. All Monte Carlo results are shown in Fig. 12.

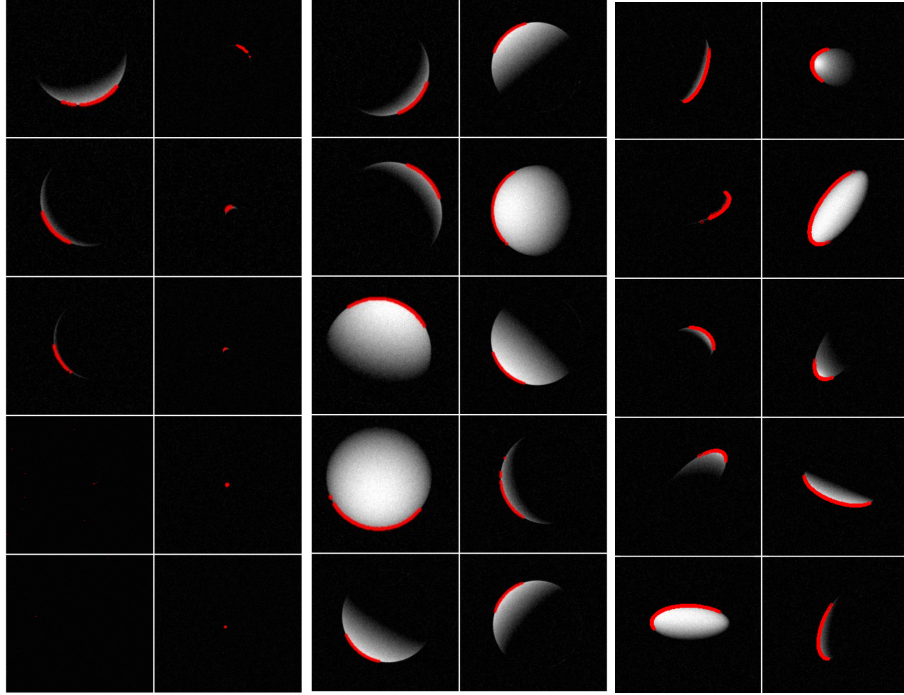


Fig. 11 Sample Image History with Detected Horizon Points from Fig. 10 for Case Without Observability-constrained control (Left), and With Observability-constrained control using Spherical Primary (Middle), and $[2.5 \ 1 \ 1]$ Ellipsoid Primary (Right) Ordered Top-Bottom, then Left-Right.

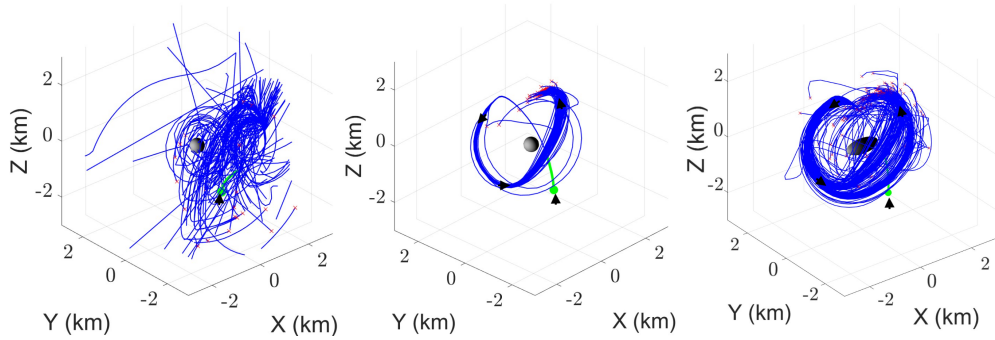


Fig. 12 Monte Carlo Simulation of 200 True Trajectories using Basic Lyapunov controller (Left), Observability-constrained Lyapunov controller with Spherical (Middle) and $[2.5 \ 1 \ 1]$ Ellipsoid Primary (Right). Initial position (green circle), final position (red cross) and orbital direction (black arrows) indicated.

6.2 Approach and Circularization Scenario

Beyond the orbit maintenance scenario, it is important to demonstrate the effectiveness of this controller in a greater variety of situations, including those starting further

away from the asteroid. Therefore, we test this algorithm in a specific test case where we approach the asteroid from just within the effective range of horizon-based OpNav determined in Section 5.1. The controller aims to circularize around the asteroid and executes maneuvers accordingly. The initial conditions in cartesian terms are ${}^H\mathbf{r} = [0, 0, -4.5964]^\top$ km and ${}^H\mathbf{v} = [-4.8927, 0, 2.4464]^\top$ mm/s. The same initial covariance is used as in Section 6.1. The gain found to return the best performance for the controller in this particular test case is:

$$K_2 = \text{diag}(10^{-3}, 10^{-3}, 10^{-3}, 10^{-3}, 10^{-7}, 10^{-7}) \quad (34)$$

The penalty function parameters chosen are identical to those from Section 6.1, except the weight for the cone constraint is increased to $\omega_3 = 100$. This leads to better performance in avoiding the poor observability region at the larger scale of this scenario.

We repeat a comparison between the regular (Fig. 13) and observability-constrained (Fig. 14) controllers. The figures depict the spacecraft’s true trajectory, OpNav measurement, EKF position estimate and a visualization of the keep-out cone. The result matches the outcome from Section 6.1 with the observability-constrained controller avoiding the keep-out cone and successfully circularizing around the asteroid. The regular controller’s true and EKF-estimated trajectories diverge since it enters the keep-out cone and produces faulty measurements. An additional test with the observability-constrained controller was executed with a $[2.5 \ 1 \ 1]$ ellipsoid using the rotation parameters of Bennu and an approximation from its known mean radius.

Camera snapshots of each case with the detected horizon points highlighted in red can be seen in Fig. 15. The observations are mostly similar to those from Section 6.1. The difference is that the lit limb is much smaller at the start of the simulation and grows as the spacecraft approaches the asteroid. The measurement and controller perform well under such variable conditions.

The maximum fuel consumption to execute the control used during this trajectory was calculated to be approximately 0.1 kg over 5 days, which is a reasonable quantity within its fuel reserves. This calculation was done using the same method from Section 6.1.

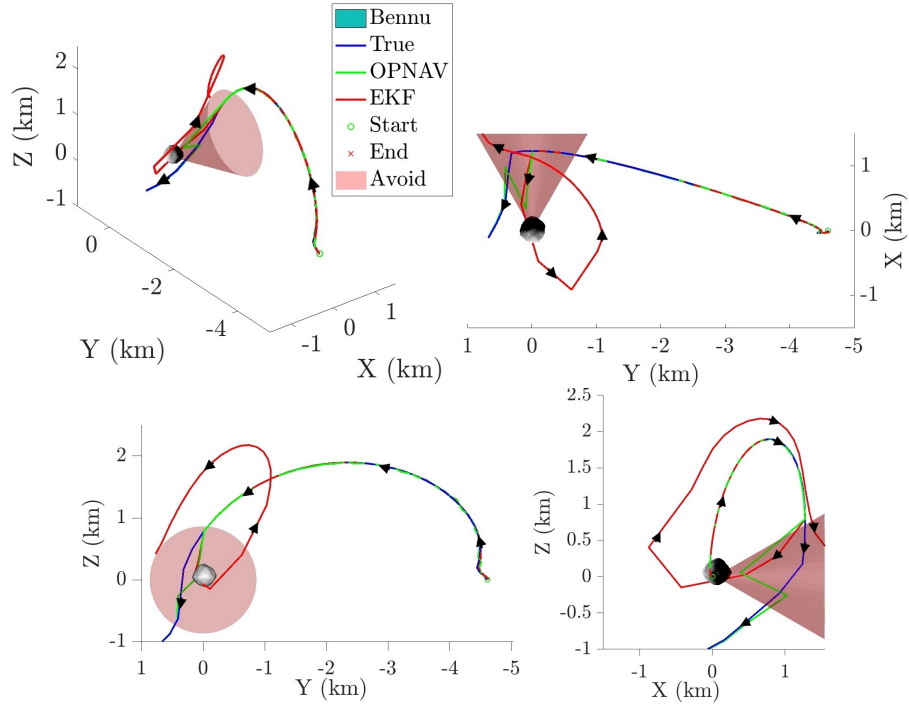


Fig. 13 True (blue), OpNav measurement (green), EKF-estimated (red) Trajectories and keep-out cone (shaded red) without Observability-constrained Penalty Lyapunov control around Benu shown in 4 views. Initial position (green circle), final position (red cross) and orbital direction (black arrows) indicated.

6.2.1 Monte Carlo Analysis

The monte carlo analysis is repeated for the approach and circularization scenario. The same settings from Section 6.1.1 are used, with initial position standard deviation of $\sigma = 30$ meters and 200 iterations. The regular controller succeeds in 68 out of 200 iterations for a success rate of 34%. The EKF and true dynamics diverge often and lead to the spacecraft either crashing into the asteroid or traveling out of the system. The observability-constrained Lyapunov controller shows improved performance with a success rate of 181 out of 200 iterations for a success rate of 90.5%. Meanwhile, the same case with a $[2.5 \ 1 \ 1]$ ellipsoid succeeds for 168 out of 200 iterations for a success rate of 84%. This supports the consistent performance benefit of the observability-constrained controller across multiple scenarios. The controller is shown to be useful in approach scenario at larger distance, where the ellipsoid assumption better holds. While the performance degrades for the ellipsoid test in this case as well, it maintains better performance than the regular controller. All Monte Carlo results are shown in Fig. 16.

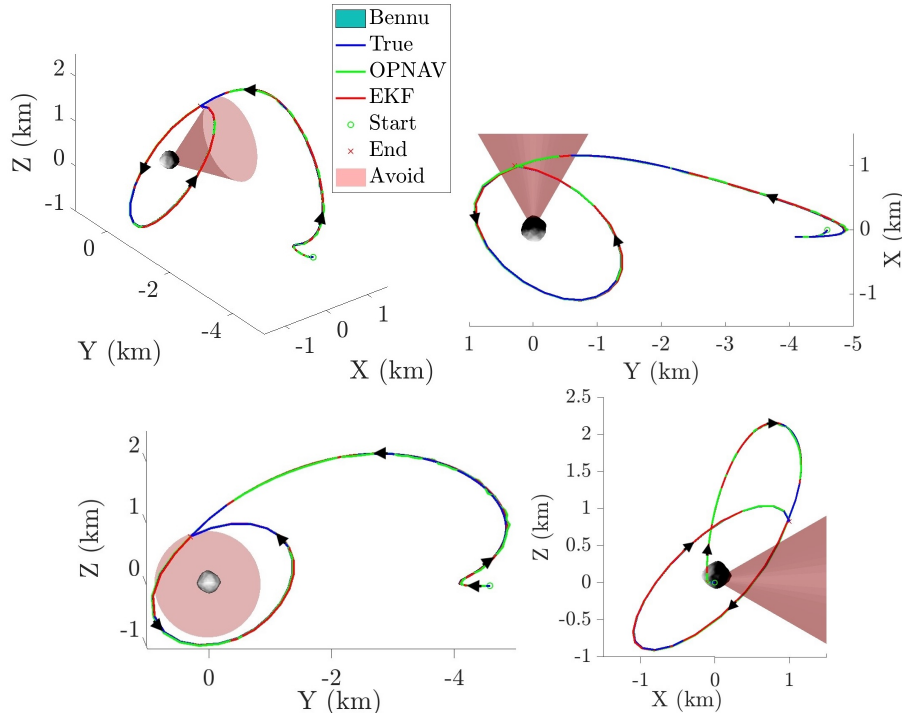


Fig. 14 True (blue), OpNav measurement (green), EKF-estimated (red) Trajectories and keep-out cone (shaded red) with Observability-constrained Penalty Lyapunov control around Bennu shown in 4 views. Initial position (green circle), final position (red cross) and orbital direction (black arrows) indicated.

7 Discussion

This paper presents a promising approach to autonomous asteroid OpNav using a Lyapunov controller with path constraints for observability-constrained maneuvers. The approach offers a combination of OpNav methods, state estimation, and control, especially when navigating challenging environments around asteroids.

The developed controller overcomes the limited applicability of the Horizon-based OpNav algorithm under extreme lighting conditions for asteroid navigation. When the spacecraft is positioned behind the asteroid's dark side, there is poor observability for the system due to an undetectable horizon, potentially leading to inaccurate state estimations. The observability-constrained controller concept allows the design of a control scheme that ensures a spacecraft follows a trajectory that avoids these faulty measurements. This method is better than simply discarding poor measurements, which may lead to an extended gap without measurements, causing the state estimate to diverge.

This research also develops an understanding of the applicability of horizon-based OpNav as a measurement for asteroid navigation. It is found that it is effective up to

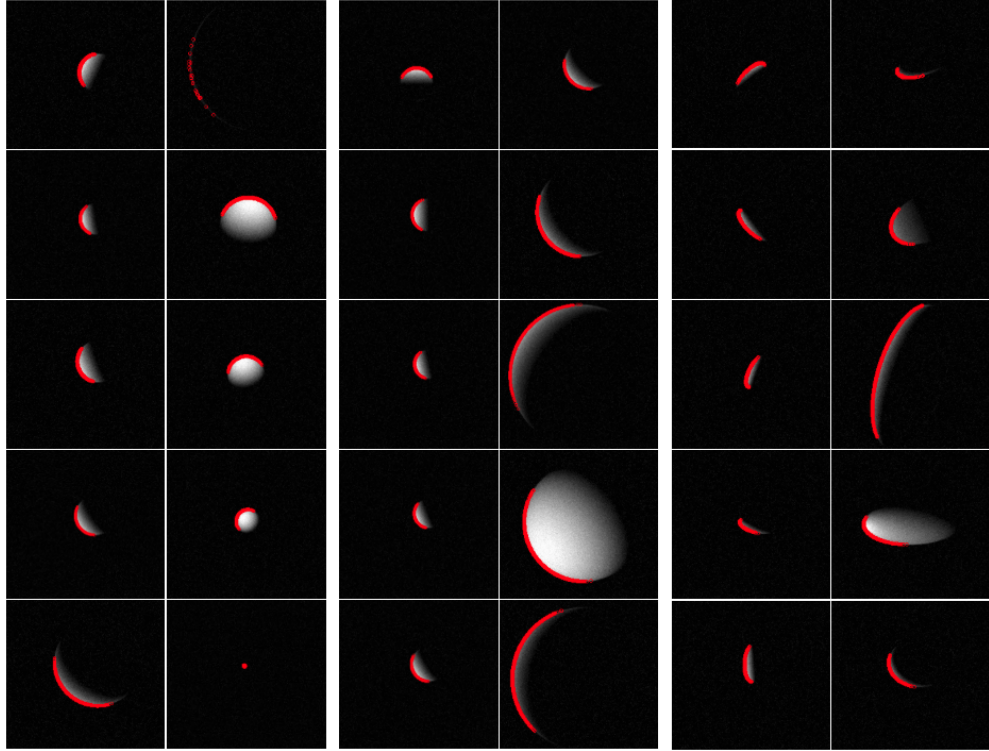


Fig. 15 Sample Image History with Detected Horizon Points from Fig. 13 for Case Without Observability-constrained control (Left), and Fig. 14 for Cases With Observability-constrained control using Spherical Primary (Middle), and [2.5 1 1] Ellipsoid Primary (Right) Ordered Top-Bottom, then Left-Right.

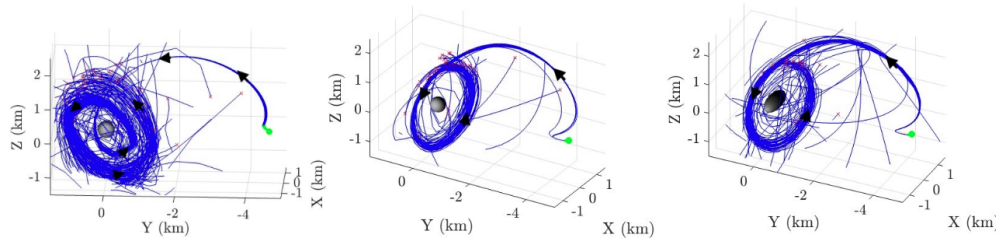


Fig. 16 Monte Carlo Simulation of 200 True Trajectories using Basic Lyapunov controller (Left), Observability-constrained Lyapunov controller with Spherical (Middle) and [2.5 1 1] Ellipsoid Primary (Right). Initial position (green circle), final position (red cross) and orbital direction (black arrows) indicated.

a range of 25-30 times a target asteroid's radius, outside of a cone with a 30-degree half-angle from either straight-on or dark-side viewing, and displays reasonable performance with an ellipsoidal target body up to a [5,1,1] shape axis ratio. While the

image generation method used for this research is quick, generating each image at an average rate of 0.3 seconds is the primary computational restriction for the Monte Carlo simulation.

While effective under certain conditions, the implementation shows a divergence in scenarios with extreme noise, highly nonlinear dynamics, or erroneous initial states. This highlights either a possible need for further tuning and refinement of the EKF or a limitation due to the controller not accounting for navigation errors. However, it is effective within realistic bounds and expectations of these parameters that would be found in an actual space mission. The system demonstrates effective state estimation for both spherical and ellipsoidal bodies while the spacecraft is in stable orbits. However, the performance deteriorates with more complex, nonlinear trajectories or highly elliptical asteroids.

This solution does not yet provide sufficient observability for shape estimation, particularly when attempting to estimate the radius or shape ratios of the asteroid. More information is required for the filter to estimate these parameters successfully. Two options are through additional optical methods to infer properties such as the asteroid's triaxial ellipsoid shape ratios and differential imaging to determine velocity to make the system observable in terms of shape estimation. These methods are a current area of investigation and the next step in this algorithm's development.

The current approach to trajectory generation through Lyapunov control has shown significant improvements. However, testing it against a wider range of scenarios with varying tuning parameters is vital to determine a more intuitive approach to adapting the controller to any desired mission profile. Formulating an objective function that analytically quantifies observability within the Lyapunov controller rather than using a path constraint could lead to even more robust and stable performance. Another avenue for investigation is the OpNav measurement interval and how it may affect the controller's success rate. This may create a baseline for designing the spacecraft sensor to balance measurement cost and state estimate accuracy. Additionally, the gain must be very precisely tuned, as the asteroid environment requires precise control. It is very sensitive and, therefore, highly susceptible to minor gain or control profile changes. Potential improvements to the algorithm include refining controller gain settings for different mission profiles and exploring additional optical methods to enhance shape and state estimation simultaneously.

This method of using a horizon-based OpNav with observability-constrained Lyapunov control may offer a more computationally efficient and autonomous option for the early mission approach phase. It reduces the need for human-in-the-loop OpNav since the spacecraft can navigate itself to attain useful measurements as it approaches the asteroid. Furthermore, it has computation efficiency and accuracy advantages over other OpNav methods for a wider range of observable distances and angles. However, it is important to note that the proposition to use horizon-based OpNav with observability-constrained maneuvers is not intended to replace the

methodologies used in existing space missions fully. Instead, we offer an additional method that is feasible to implement to improve mission efficiency and safety. This is because the observability constraint ensures continuous and reliable measurements at all mission stages while within the horizon-based OpNav range. The Lyapunov control and state estimation algorithms combined with the OpNav enable autonomy across the early mission approach to close proximity phases of an asteroid mission. There is potential for future work to extend its applicability, improve performance in extreme conditions, and develop more sophisticated state and shape estimation methods. These improvements are critical for expanding the system’s use in future deep space exploration missions.

8 Conclusion

This research successfully demonstrates a robust autonomous navigation and control method for spacecraft approaching or conducting operations near asteroids. A comprehensive simulation environment is developed that considers spacecraft dynamics around an asteroid, synthetic asteroid imaging and processing, horizon-based OpNav, EKF, and observability-constrained Lyapunov control. The novel contribution is a Lyapunov controller with path constraints to improve horizon-based OpNav measurement observability. Its effectiveness has been demonstrated by testing its stability when combined with EKF-based state estimation within acceptable error bounds. The validation with a simplified model of Bennu as a benchmark highlights the reliable test of its capabilities in this application. The system’s robustness in varying scenarios, including near-linear hyperbolic trajectories, flybys, and various orbit transfers, highlights its potential for broader applications in autonomous asteroid exploration.

Appendix A Path Constraint Partial Derivatives

This section extends the derivation in Section 4.1 by computing the partial derivatives of the path constraints. The path constraint partial derivatives in terms of Milankovitch orbital elements are as follows:

$$\frac{dg_1({}^H\mathbf{x}_{\text{slow}})}{d{}^H\mathbf{x}_{\text{slow}}} = \begin{bmatrix} -\frac{(2h_1+h_2^2+h_3^2)}{\mu} \frac{1}{1-e} \\ -\frac{(2h_2+h_1^2+h_3^2)}{\mu} \frac{1}{1-e} \\ -\frac{(2h_3+h_2^2+h_1^2)}{\mu} \frac{1}{1-e} \\ -\frac{e_1 h^2}{\mu e(e-1)^2} \\ -\frac{e_2 h^2}{\mu e(e-1)^2} \\ -\frac{e_3 h^2}{\mu e(e-1)^2} \end{bmatrix} \quad (\text{A1})$$

$$\frac{dg_2({}^H \mathbf{x}_{\text{slow}})}{d{}^H \mathbf{x}_{\text{slow}}} = \begin{bmatrix} -\frac{(2h_1+h_2^2+h_3^2)}{\mu} \frac{1}{1-e} \\ -\frac{(2h_2+h_1^2+h_3^2)}{\mu} \frac{1}{1-e} \\ -\frac{(2h_3+h_2^2+h_1^2)}{\mu} \frac{1}{1-e} \\ -\frac{e_1 h^2}{\mu e(e-1)^2} \\ -\frac{e_2 h^2}{\mu e(e-1)^2} \\ -\frac{e_3 h^2}{\mu e(e-1)^2} \end{bmatrix} \quad (\text{A2})$$

$$\frac{dg_3({}^H \mathbf{x}_{\text{slow}})}{d{}^H \mathbf{x}_{\text{slow}}} = \left[\frac{h_2^2 + h_3^2}{h^{1.5}}, -\frac{h_1 h_2}{h^{1.5}}, -\frac{h_1 h_3}{h^{1.5}}, 0_{3 \times 1} \right] \quad (\text{A3})$$

h_2 and h_3 are the components of angular momentum in the y-axis and z-axis direction respectively, in the Hill frame.

Appendix B Controller Gain Tuning Guidelines

Since the gains determined for the controller used in this research are for specific test cases with Bennu, it is imperative to develop guidelines to derive it for different scenarios to make it useful for diverse missions. After investigating the relations between the gains and the controller performance, the following observations and guidelines are made:

1. The base gain magnitude used is 10^{-3} where the gains in the angular momentum vector and eccentricity vector are tweaked to a different ratio across varying axes depending on in which direction the control is intended to be imparted. This value seems to offer a critical balance and match with a few orders of magnitude below the angular momentum and eccentricity values used in this research, allowing precise changes. The eccentricity gains never exceed the angular momentum, as this is found to create unstable results.
2. The gain matrix used in the first scenario is used for stationkeeping. Here, the angular momentum in the x direction in the Hill frame has a higher gain, and the eccentricity in the x and y directions in the Hill frame has lower gains. The intuition is that this allows the controller to readily tweak the spacecraft's position and counter the effect of SRP. This distinction in gain may not be required for a different application where the dynamics are more balanced.
3. The gain used in the second scenario is intended to focus on circularization. Here, the eccentricity in the y and z direction in the Hill frame is set to a lower gain, which allows the controller to rapidly adjust the eccentricity in the x direction in the Hill frame to circularize the orbit while maintaining the spacecraft in the desired orbital plane. Depending on the nature of the mission and target orbit, different axes can have modified gains to execute transfers within a desired plane.

This Lyapunov controller formulation may be adapted for different use cases using these observations. Results demonstrating the effectiveness of these gains can be seen in Section 6.

Declarations

Conflict of Interest

On behalf of all authors, the corresponding author states that there is no conflict of interest.

References

- [1] Yada, T., Abe, M., Okada, T., Nakato, A., Yogata, K., Miyazaki, A., Hatakeda, K., Kumagai, K., Nishimura, M., Hitomi, Y., Soejima, H., Yoshitake, M., Iwamae, A., Furuya, S., Uesugi, M., Karouji, Y., Usui, T., Hayashi, T., Yamamoto, D., Fukai, R., Sugita, S., Cho, Y., Yumoto, K., Yabe, Y., Bibring, J.P., Pilonget, C., Hamm, V., Brunetto, R., Riu, L., Lourit, L., Loizeau, D., Lequertier, G., Moussi-Soffys, A., Tachibana, S., Sawada, H., Okazaki, R., Takano, Y., Sakamoto, K., Miura, Y.N., Yano, H., Ireland, T.R., Yamada, T., Fujimoto, M., Kitazato, K., Namiki, N., Arakawa, M., Hirata, N., Yurimoto, H., Nakamura, T., Noguchi, T., Yabuta, H., Naraoka, H., Ito, M., Nakamura, E., Uesugi, K., Kobayashi, K., Michikami, T., Kikuchi, H., Hirata, N., Ishihara, Y., Matsumoto, K., Noda, H., Noguchi, R., Shimaki, Y., Shirai, K., Ogawa, K., Wada, K., Senshu, H., Yamamoto, Y., Morota, T., Honda, R., Honda, C., Yokota, Y., Matsuoka, M., Sakatani, N., Tatsumi, E., Miura, A., Yamada, M., Fujii, A., Hirose, C., Hosoda, S., Ikeda, H., Iwata, T., Kikuchi, S., Mimasu, Y., Mori, O., Ogawa, N., Ono, G., Shimada, T., Soldini, S., Takahashi, T., Takei, Y., Takeuchi, H., Tsukizaki, R., Yoshikawa, K., Terui, F., Nakazawa, S., Tanaka, S., Saiki, T., Yoshikawa, M., Watanabe, S., Tsuda, Y.: Preliminary analysis of the hayabusa2 samples returned from c-type asteroid ryugu. *Nature Astronomy* **6** (2022) <https://doi.org/10.1038/s41550-021-01550-6>
- [2] Daly, M.G., Barnouin, O.S., Seabrook, J.A., Roberts, J., Dickinson, C., Walsh, K.J., Jawin, E.R., Palmer, E.E., Gaskell, R., Weirich, J., Haltigin, T., Gaudreau, D., Brunet, C., Cunningham, G., Michel, P., Zhang, Y., Ballouz, R.L., Neumann, G., Perry, M.E., Philpott, L., Asad, M.M.A., Johnson, C.L., Adam, C.D., Leonard, J.M., Geeraert, J.L., Getzandanner, K., Nolan, M.C., Daly, R.T., Bierhaus, E.B., Mazarico, E., Rozitis, B., Ryan, A.J., Dellaguistina, D.N., Rizk, B., Susorney, H.C.M., Enos, H.L., Lauretta, D.S.: Hemispherical differences in the shape and topography of asteroid (101955) bennu. *Science Advances* **6** (2020) <https://doi.org/10.1126/sciadv.abd3649>
- [3] Adam, C.D., Antreasian, P.G., Carcich, B.T., Leonard, J.M., Lessac-Chenen, E.J., McCarthy, L.K., Nelson, D.S., Pelgrift, J.Y., Sahr, E.M., Wibben, D.R., Knutson, S., Enos, H.L., Harshman, K., Hergenrother, C., Kidd, J.N., Lambert, D., Polit, A.T., Rizk, B., Lauretta, D.S., Billett, O., Lefevre, M., Moreau, M.C., Bos, B.J., Calloway, A., Castro, N., Cavaluzzi, J., Getzandanner, K.M., Mink, R., Poland, D.: Concept of operations for osiris-rex optical navigation image planning. In: *AIAA Science and Technology Forum and Exposition, AIAA SciTech Forum 2022* (2022). <https://doi.org/10.2514/6.2022-1569>
- [4] Watanabe, S., Tsuda, Y., Yoshikawa, M., Tanaka, S., Saiki, T., Nakazawa,

- S.: Hayabusa2 Mission Overview (2017). <https://doi.org/10.1007/s11214-017-0377-1>
- [5] Michel, P., Kueppers, M., Sierks, H., Carnelli, I., Cheng, A.F., Mellab, K., Granvik, M., Kestilä, A., Kohout, T., Muinonen, K., Näsilä, A., Penttilä, A., Tikka, T., Tortora, P., Ciarletti, V., Hérique, A., Murdoch, N., Asphaug, E., Rivkin, A., Barnouin, O., Bagatin, A.C., Pravec, P., Richardson, D.C., Schwartz, S.R., Tsiganis, K., Ulamec, S., Karatekin, O.: European component of the aida mission to a binary asteroid: Characterization and interpretation of the impact of the dart mission. *Advances in Space Research* **62** (2018) <https://doi.org/10.1016/j.asr.2017.12.020>
 - [6] Levison, H.F., Olkin, C.B., Noll, K.S., Marchi, S., Bell, J.F., Bierhaus, E., Binzel, R., Bottke, W., Britt, D., Brown, M., Buie, M., Christensen, P., Emery, J., Grundy, W., Hamilton, V.E., Howett, C., Mottola, S., Pätzold, M., Reuter, D., Spencer, J., Statler, T.S., Stern, S.A., Sunshine, J., Weaver, H., Wong, I.: Lucy mission to the Trojan asteroids: Science goals (2021). <https://doi.org/10.3847/PSJ/abf840>
 - [7] Qi, D.C., Oguri, K.: Analysis of autonomous orbit determination in various near-moon periodic orbits. *Journal of the Astronautical Sciences* **70** (2023) <https://doi.org/10.1007/s40295-023-00415-6>
 - [8] Ning, X., Gui, M., Fang, J., Dai, Y., Liu, G.: A novel differential doppler measurement-aided autonomous celestial navigation method for spacecraft during approach phase. *IEEE Transactions on Aerospace and Electronic Systems* **53** (2017) <https://doi.org/10.1109/TAES.2017.2651558>
 - [9] Christian, J.A.: Optical navigation using planet's centroid and apparent diameter in image. *Journal of Guidance, Control, and Dynamics* **38** (2015) <https://doi.org/10.2514/1.G000872>
 - [10] McMahon, J.W., Scheeres, D.J., Berry, K.: Asteroid proximity navigation using direct altimetry measurements. In: *Advances in the Astronautical Sciences*, vol. 152 (2014)
 - [11] Woods, J.O., Christian, J.A.: Lidar-based relative navigation with respect to non-cooperative objects. *Acta Astronautica* **126** (2016) <https://doi.org/10.1016/j.actaastro.2016.05.007>
 - [12] Liounis, A.J., Getzandanner, K.: OPERATIONAL PERFORMANCE OF LIMB-BASED NAVIGATION FROM OSIRIS-REX AT BENNU. In: *Space Imaging Workshop*
 - [13] Villa, J., Osmundson, A., Hockman, B., Morrell, B., Lubey, D., Bayard, D., McMahon, J., Nesnas, I.A.: Light-robust pole-from-silhouette algorithm and visual-hull estimation for autonomous optical navigation to an unknown small body. *AAS GNC Conference* (2021)
 - [14] Ogawa, N., Terui, F., Mimasu, Y., Yoshikawa, K., Ono, G., Yasuda, S., Matsushima, K., Masuda, T., Hihara, H., Sano, J., Matsuhisa, T., Danno, S., Yamada, M., Yokota, Y., Takei, Y., Saiki, T., Tsuda, Y.: Image-based autonomous navigation of hayabusa2 using artificial landmarks: The design and brief in-flight results of the first landing on asteroid ryugu. *Astrodynamics* **4** (2020) <https://doi.org/10.1007/s42064-020-0070-0>

- [15] McCarthy, L.K., Adam, C.D., Leonard, J.M., Antresian, P.G., Nelson, D.S., Sahr, E.M., Pelgrift, J.Y., Lessac-Chennen, E.J., Geeraert, J.L., Lauretta, D.S.: Osiris-rex landmark optical navigation performance during orbital and close proximity operations at asteroid (101955) bennu. In: AIAA Science and Technology Forum and Exposition, AIAA SciTech Forum 2022 (2022). <https://doi.org/10.2514/6.2022-2520>
- [16] Christian, J.A.: A tutorial on horizon-based optical navigation and attitude determination with space imaging systems. *IEEE Access* **9** (2021) <https://doi.org/10.1109/ACCESS.2021.3051914>
- [17] Oguri, K., McMahon, J.W.: Risk-aware mission design for in situ asteroid exploration under uncertainty. In: 2021 IEEE Aerospace Conference (50100), pp. 1–17. <https://doi.org/10.1109/AERO50100.2021.9438479>
- [18] Oguri, K., McMahon, J.: Robust spacecraft guidance around small bodies under uncertainty: Stochastic optimal control approach **44** <https://doi.org/10.2514/1.G005426>
- [19] Batista Negri, R., Prado, A.F.B.A.: Autonomous and robust orbit-keeping for small-body missions **45**(3), 587–598 <https://doi.org/10.2514/1.G005863>. Publisher: American Institute of Aeronautics and Astronautics .eprint: <https://doi.org/10.2514/1.G005863>. Accessed 2025-01-06
- [20] Ishizuka, T., Lizy-Destrez, S., Ozaki, N.: ASTEROID RENDEZVOUS TRAJECTORY OPTIMIZATION AND IMPACT OF UNCERTAINTIES. In: 28th International Symposium on Space Flight Dynamics ISSFD
- [21] Ishizuka, T., Lizy-Destrez, S., Ozaki, N., Oguri, K.: Robust trajectory optimization for autonomous asteroid rendezvous. In: 73rd International Astronomical Congress (IAC)
- [22] Boone, S., Ishizuka, T., Lizy-Destrez, S.: Stochastic spacecraft maneuver design around small bodies using convex formulations. In: 2024 AAS GN&C Conference
- [23] Liu, C., Yang, H., Li, S., Li, J.: Convex optimization of stochastic path-constrained trajectories near asteroids **153**, 109463 <https://doi.org/10.1016/j.ast.2024.109463>. Accessed 2025-01-06
- [24] Wang, W., Mengali, G., Quarta, A.A., Baoyin, H.: Spacecraft relative motion control near an asteroid with uncertainties: A lyapunov redesign approach **60**(4), 4507–4517 <https://doi.org/10.1109/TAES.2024.3378196>. Conference Name: IEEE Transactions on Aerospace and Electronic Systems. Accessed 2025-01-06
- [25] Oguri, K., McMahon, J.W.: Solar radiation pressure–based orbit control with application to small-body landing **43**(2), 195–211 <https://doi.org/10.2514/1.G004489>. Publisher: American Institute of Aeronautics and Astronautics. Accessed 2025-01-01
- [26] Furfaro, R.: Hovering in asteroid dynamical environments using higher-order sliding control. In: *Journal of Guidance, Control, and Dynamics*, vol. 38 (2015). <https://doi.org/10.2514/1.G000631>
- [27] Lee, K.W., Singh, S.N.: Noncertainty-equivalence adaptive attitude control of satellite orbiting around an asteroid. *Acta Astronautica* **161** (2019) <https://doi.org/10.1016/j.actaastro.2019.05.008>
- [28] Qiao, D., Zhou, X., Zhao, Z., Qin, T.: Asteroid approaching orbit optimization

- considering optical navigation observability. *IEEE Transactions on Aerospace and Electronic Systems* **58** (2022) <https://doi.org/10.1109/TAES.2022.3167653>
- [29] Pugliatti, M., Franzese, V., Topputo, F.: Data-driven image processing for onboard optical navigation around a binary asteroid. *Journal of Spacecraft and Rockets* **59** (2022) <https://doi.org/10.2514/1.A35213>
- [30] Jia, H., Zhu, S., Cui, P.: Observability-based navigation using optical and radiometric measurements for asteroid proximity. *IEEE Transactions on Aerospace and Electronic Systems* **56** (2020) <https://doi.org/10.1109/TAES.2019.2953947>
- [31] Scheeres, D.J., Marzari, F.: Spacecraft dynamics in the vicinity of a comet. *Journal of the Astronautical Sciences* **50** (2003) <https://doi.org/10.1007/bf03546329>
- [32] Scheeres, D.J.: Orbit mechanics about asteroids and comets. *Journal of Guidance, Control, and Dynamics* **35** (2012) <https://doi.org/10.2514/1.57247>
- [33] Rosengren, A.J., Scheeres, D.J.: On the milankovitch orbital elements for perturbed keplerian motion **118**(3), 197–220 <https://doi.org/10.1007/s10569-013-9530-7>
- [34] Christian, J.A., Robinson, S.B.: Noniterative horizon-based optical navigation by cholesky factorization. In: *Journal of Guidance, Control, and Dynamics*, vol. 39 (2016). <https://doi.org/10.2514/1.G000539>
- [35] Slotine, J.-J.E., Li, W.: *Applied Nonlinear Control*. Prentice-Hall, Englewood Cliffs, NJ (1991)
- [36] Schaub, H., Junkins, J.L.: *Analytical Mechanics Of Space Systems*, (2003). <https://doi.org/10.2514/4.861550>
- [37] Lauretta, D.S., DellaGiustina, D.N., Bennett, C.A., Golish, D.R., Becker, K., Balram-Knutson, S.S., Barnouin, O.S., Becker, T.L., Bottke, W.F., Boynton, W.V., Campins, H., Clark, B.E., Connolly, H.C., d’Aubigny, C.D., Dworkin, J.P., Emery, J.P., Enos, H.L., Hamilton, V.E., Hergenrother, C.W., Howell, E.S., Izawa, M.R.M., Kaplan, H.H., Nolan, M.C., Rizk, B., Roper, H.L., Scheeres, D.J., Smith, P.H., Walsh, K.J., Wolner, C.W.V.: The unexpected surface of asteroid (101955) bennu **568**(7750), 55–60 <https://doi.org/10.1038/s41586-019-1033-6> . Accessed 2024-12-09
- [38] Lauretta, D.S., Bartels, A.E., Barucci, M.A., Bierhaus, E.B., Binzel, R.P., Bottke, W.F., Campins, H., Chesley, S.R., Clark, B.C., Clark, B.E., Cloutis, E.A., Connolly, H.C., Crombie, M.K., Delbó, M., Dworkin, J.P., Emery, J.P., Glavin, D.P., Hamilton, V.E., Hergenrother, C.W., Johnson, C.L., Keller, L.P., Michel, P., Nolan, M.C., Sandford, S.A., Scheeres, D.J., Simon, A.A., Sutter, B.M., Vokrouhlický, D., Walsh, K.J.: The OSIRIS-REx target asteroid (101955) bennu: Constraints on its physical, geological, and dynamical nature from astronomical observations **50**(4), 834–849 <https://doi.org/10.1111/maps.12353> . eprint: <https://onlinelibrary.wiley.com/doi/pdf/10.1111/maps.12353>. Accessed 2024-12-09
- [39] Tricarico, P., Scheeres, D.J., French, A.S., McMahon, J.W., Brack, D.N., Leonard, J.M., Antreasian, P., Chesley, S.R., Farnocchia, D., Takahashi, Y., Mazarico, E.M., Rowlands, D., Highsmith, D., Getzandanner, K., Moreau, M., Johnson, C.L., Philpott, L., Bierhaus, E.B., Walsh, K.J., Barnouin, O.S., Palmer, E.E., Weirich, J.R., Gaskell, R.W., Daly, M.G., Seabrook, J.A., Nolan, M.C., Lauretta,

D.S.: Internal rubble properties of asteroid (101955) bennu. *Icarus* **370** (2021)
<https://doi.org/10.1016/j.icarus.2021.114665>